NSG-7610

The P-wave upper mantle structure beneath an active spreading center: the Gulf of California

Marianne C. Walck

Seismological Laboratory, California Institute of Technology,

Pasadena, California 91125

March 30, 1983

Short title: Gulf of California upper mantle structure

ABSTRACT

Detailed analysis of short-period travel time, $dT/d\Delta$ and waveform data reveals the upper mantle structure beneath an oceanic ridge to depths of 900 km. More than 1400 digital seismograms from earthquakes in Mexico and central America recorded at SCARLET yield 1753 travel times and 58 direct measurements of $dT/d\Delta$ as well as high-quality, stable waveforms. The 29 events combine to form a continuous record section from 9° to 40° with an average station spacing of less than 5 km. First the travel times are inverted using the tau method of Bessonova et al. (1974,1976); the resultant model is adjusted to agree with the experimental p-Δ values. Further constraints arise from the observed relative amplitudes of mantle phases, which are modeled by trial-and-error using WKBJ synthetic seismograms (Chapman, 1976; Wiggins, 1976). Model GCA, which is appropriate for western Mexico north of 20° latitude, is similar to existing upper mantle models for shield, tectonic-continental, and arc-trench regimes below 400 km, but differs significantly in the upper 350 km. GCA velocities are very low in this depth range; the model "catches up" to the others with a very large velocity gradient from 225 km to 390 km. This well-resolved feature is consistent with the shear-wave model TNA for western North America of Grand & Helmberger (1983). The abundant data from 20° to 30° control the detailed shape of the 660-km discontinuity. Very high velocity gradients lie both above (620-660 km) and below (661-680 km) a 2.8% velocity change.

Introduction

The nature of lateral variations in upper mantle seismic velocities is a problem of broad geophysical interest. Velocity structure determinations for many regions can place constraints on both the scale of mantle convection and the depth extent of velocity differences between continents and ocean basins. Hager & Raefsky (1981) predict large depressions of a chemical "670 km" discontinuity beneath subducted slabs if convection is confined to the upper mantle. Sipkin & Jordan (1975, 1976) suggest that lateral differences between shields and old oceans extend to 400 km depth to satisfy multiple ScS travel times, while Okal & Anderson (1975) insist that most of the differences between shields and old oceanic ScS data are explained by heterogeneity shallower than 200 km. Recent upper mantle models for continental shields (e.g. King & Calcagnile, 1976; Given & Helmberger, 1980), "young" continental regions (Johnson, 1967; England et al., 1977; Burdick & Helmberger, 1978; among others) and island arc regimes (Kanamori, 1967; Fukao, 1977) have been constructed using body waves; these models tend to converge below 200 km. Very little work has been done, however, on the important areas of ocean basins, continental rifts and spreading centers. Some surface wave studies indicate low upper mantle velocities for young oceans (Knopoff et al., 1970; Montagner & Jobert, 1981; Wielandt & Knopoff, 1982) to depths of at least 200 km. England et al. (1978) analyzed P-wave data from the North Atlantic Ocean, and Green (1978), Nolet & Mueller (1982) and Lenartowicz & Albert (1980) studied the African rift region, for which very slow teleseismic travel times have also been documented. The detailed characteristics of the upper mantle to 1000 km beneath spreading centers, however, are unknown.

We have investigated the upper mantle P-wave velocities under the Gulf of California spreading center. Mexican earthquakes recorded at the California

Institute of Technology - U.S. Geological Survey Southern California Seismic Network (SCARLET) provide a unique, dense, high-quality data set. The narrow azimuthal range of the epicentral distribution results in a nearly ideal data profile. We exploit the large amount of travel-time, apparent velocity ($dT/d\Delta$) and waveform data in the modeling process. While the travel times control the model's gross integral properties, the $dT/d\Delta$ measurements provide information about the absolute velocities at the rays' turning points. The relative amplitudes of phases are most sensitive to the velocity gradients near the bottoming points. We combine these data by first inverting the travel times, perturbing that model to fit the $p - \Delta$ data, and then performing trial-and-error synthetic seismogram modeling to fit the short-period waveforms. The final model satisfies all three data sets. Thus our model has more resolvable detail than those derived from travel times alone (e.g. Hales, 1972; Massé, 1973, 1974; Green, 1978) or from array studies utilizing travel times and apparent phase velocities but which contain no waveform analysis (Johnson, 1967; Simpson et al., 1974; Ram & Mereu, 1977; King & Calcagnile, 1976; Ram et al., 1978; England et al., 1977, 1978; and others). In addition, our high-quality, dense array data allows better resolution than discrete source-receiver waveform studies such as Helmberger & Wiggins(1971), Wiggins & Helmberger (1973), Dey-Sarkar & Wiggins (1976) and McMechan (1979). While short-period waveforms are not as stable as the equivalent long-period data, teleseismic waveforms recorded across the 5° aperture of SCARLET are very reproducible, indicating good stability for simple events. Our final model represents a synthesis of differing constraints and results in a well-resolved, detailed view of the upper mantle under or near an active oceanic ridge.

The Data Set

The seismically active areas of the Gulf of California, Rivera Fracture Zone, East Pacific Rise, and Middle America Trench are the source regions for this study. Figure 1 illustrates the experimental geometry, including 2° arcs drawn at the travel path midpoints of the 22 events at distances of less than 30°. Clearly, the upper mantle sampled by these earthquakes is not influenced by the Middle America Trench, but represents the Gulf of California and adjacent extensional areas. The events occurring on the spreading centers and fracture zones have strike-slip mechanisms oriented unfavorably for P-wave radiation to SCARLET, and tend to have complicated source signatures. Most of these events are closer than 20°. The subduction zone earthquakes, on the other hand, at epicentral distances greater than 18°, are dip-slip events, which produce ample P-wave energy and are often simple in character. The events range in distance from 9° to 40° and occur in the narrow event-station azimuth band of 310° to 345°. Varying in depth from 10 km to 150 km, they have body-wave magnitudes of 5.0 to 6.3. All events occurred between September, 1977 and December, 1979, and are listed with the PDE epicentral information in Table 1.

Each earthquake is recorded by the short-period vertical, digital, triggered CEDAR system (Johnson, 1979) at the California Institute of Technology. In its current configuration SCARLET has more than 200 stations; from 1977 to 1979 a well-recorded teleseism would trigger 120 stations, about 60 of which fit the criteria for inclusion in the data set (Figure 2). Elongate in the northwest-southeast direction, the array has an aperture of 5° and irregular station spacing averaging 25 km. Although the array stations have varying instrumentation, the responses are very similar at 1 Hz, the predominant frequency of the teleseismic signal.

Over 1400 digital seismograms were collected from the 29 events, yielding 1753 travel times including 438 which are secondary arrivals. In addition, we obtained 58 direct measurements of the ray parameter, $dT/d\Delta$, spanning the 31° distance range. Figures 3, 4, 5, and 6 show examples of record sections for several events at different distances. Because SCARLET is not well-calibrated, only relative amplitudes are used, and each trace is scaled to its maximum amplitude. Adjacent records are very similar, indicating excellent waveform stability across the array. The events in Figures 4, 5, and 6 are all simple and impulsive, allowing unambiguous selection of secondary phases. Each record section covers 4° - 5° in distance and collapses about 10° of azimuthal variation onto a plane. Distances in Figures 3 - 6 are not corrected for event depth. Portions of interesting upper mantle triplication phases are visible for each event, but a more complete picture is obtained by combining the 10 cleanest events covering the entire distance range into one record section (Figure 7). This representation contains 477 depth-corrected seismograms with an average data spacing of 8 km. Inclusion of all available data reduces the spacing to less than 5 km. Secondary arrivals from both the "400 km" and "670 km" discontinuities are seen clearly from 14° to 28°. This high-quality data prompts careful and complete data analysis to insure a robust, detailed upper mantle model.

Data Preparation and Analysis

Receiver structure in southern California

An area of complex geology and present-day tectonic activity, southern California has a complicated, heterogeneous crust and uppermost mantle structure which affects incoming teleseismic signals. The large amount of available data (both local and teleseismic events) have prompted several studies probing the nature of the receiver structure beneath SCARLET. Kanamori & Hadley (1975) reported on the region's upper crustal velocities; Lamanuzzi (1981) and Hearn (1983) have investigated gross crustal and upper mantle properties using Pn travel times. Teleseismic P arrivals were used in upper mantle heterogeneity studies by Hadley & Kanamori (1977), Raikes & Hadley (1979), Raikes (1980) and Walck & Minster (1982). The spatial pattern of the strong azimuthal variation of teleseismic P-residuals (Raikes, 1980) is consistent with a high-velocity body in the upper mantle beneath the Transverse Ranges in southern California, first proposed by Hadley & Kanamori (1977) and verified by Walck & Minster (1982).

Correcting for near-receiver velocity variations in a multi-azimuth data set in this complex area could require detailed ray tracing, but for our "single" azimuth data a simpler approach was adopted. We constructed station corrections derived from travel times of more distant ($30° < \Delta < 40°$) central American earthquakes (Figure 1, Table 1) in the same azimuth band. These events are free of complicating upper mantle phases, yet the rays are incident at the receiver at angles similar to the closer events. Planes are fit to arrival times using least-squares for several large, impulsive events; the station corrections are the averaged station residuals from the plane-predicted arrival times. The procedure assumes that 1) constant corrections are appropriate over the entire 30° azimuth spread and 2) the travel-time curve is smooth beyond 30° in

distance.

The seven distant events have a total azimuth range of only 8° and are remarkably consistent: 96 stations have average residual values with standard deviations of less than 0.10 s (shown in Figure 2). Our empirical corrections include effects of both local structure and elevation, and are applied to all the data to reduce travel-time scatter and aid in identification of secondary phases. An example of a record section before and after application of the empirical corrections is shown in Figure 8.

We might expect a close correlation between the empirical adjustments and Raikes' (1980) teleseismic residuals for the same azimuth range. Although her data are from more distant ($\Delta \sim 55°$) earthquakes, and are single-station residuals instead of deviations to the array least-squares plane, the contour plots of the two residual sets (Figure 9) are similar in shape. The difference in absolute magnitude of the residuals occurs because Raikes' (1980) residuals are referenced to an individual station, GSC, instead of the plane average and have been corrected for elevation, basin sediments and large-scale Moho depth variations.

Travel Times

The 29 events are retrieved from magnetic tape storage and the travel times hand-picked with accuracy that approaches the digitization interval, .02 s. Both direct picking and cross-correlation techniques were tested with nearly identical results. The results displayed here are for hand-picked times. Many records are low-gain or noisy; about one-half of the original seismograms are ultimately rejected, leaving about 60 records for each event. Each travel time is corrected for ellipticity, for depth (using the Jeffreys upper mantle model) and with the empirical station correction. The 1753 travel times provide a continuous curve from 9° - 40° (Figure 10). Errors in the earthquakes' hypocenters and

origin times still cause considerable scatter in the travel time data. These uncertainties are removed by applying baseline shifts based on the average of JB residuals in completely overlapping 0.5° distance windows. These shifts preserve the shape of the observed travel time curve, yet reduce the data scatter to 0.4 s; the agreement in differential travel times for secondary phases is excellent (Figure 10b).

Apparent Velocities

The numerous high-quality travel times allow calculation of many reliable $dT/d\Delta$, or ray parameter, estimates for both primary and later arrivals. The standard plane-fitting technique (e.g. Manchee & Weichert, 1968) for phase velocity determination is used on the empirically corrected but not baseline-shifted times. Because of the great size of the array, the earth's sphericity is taken into account according to the procedure outlined by Walck & Minster (1982). Before computation begins, each event record section is visually inspected for changes in the travel-time slope with distance. When such a change exists, the array is divided into two sections and two ray parameter estimates are made. Measurements of $dT/d\Delta$ made with only part of the array are still stable and accurate because of the network's large number of stations.

We obtained 58 p - Δ points (Table 1) shown in Figure 11. Fourteen of the measurements are determined from later arrivals. The values have low error estimates, are stable and exhibit little scatter. Some smoothing of changes in apparent phase velocity could occur over SCARLET's 5° aperture. To test for this, the network is split in half by a northeast-southwest trending line and all p - Δ points redetermined and compared to the whole-array estimates. We found no significant differences between the 77-point split-array data set and the 58-point whole-array group. The excellent travel-time and $dT/d\Delta$ data permit standard

inversions to find a reasonable starting model for synthetic seismogram modeling of the structure.

Inversions

Travel times

Instead of inverting the p - Δ curve with the classic Wiechert-Herglotz formula, we performed a direct travel time inversion using the tau method of Bessonova et al. (1974,1976) which has advantageous statistical properties. The quantity

$$\tau(p) = T - pX$$

where T is travel time, p is ray parameter and X is epicentral distance is calculated directly from the travel time data. For a fixed ray parameter, p_0, $\tau(p_0)$ is the extremum of the function $\tau(X)_{p=p_0}$ along a single travel time branch (Bessonova et al., 1974, 1976). To statistically determine $\tau(p_0)$, we assume that $\tau(X)_{p=p_0}$ is a constant for a small window in X centered on X_0, the distance at which $\tau(X)$ is an extremum. Then $\tau(p_0)$ is a simple average of all the $\tau(X)_{p=p_0}$ data points in that X interval (see Figure 5 in Bessonova et al., 1976). A confidence interval, δ_0, for the estimate is given by

$$\delta_0 = n^{-1/2} s\ t_\alpha (n-1)$$

Here n is the number of observations, s is the standard deviation of $\tau(p_0)$ and $t_\alpha (n-1)$ are values for the Student's distribution with n-1 degrees of freedom (see Bessonova et al., 1976 for details). The statistical confidence limit is important in assessing the model uncertainty.

The Mexico data set yields 33 values for τ in the p range 8.3 s deg $^{-1}$ to 14.0 s deg $^{-1}$, which roughly corresponds to distances of 10° to 40°. Typical values for n and δ_τ are 50 and .20 s, respectively, although some values are much better determined than others. After assuming a crustal model, the tau data was inverted first for the best single velocity model, and then, incorporating the uncertainty values, for the extremal bounds allowed by the travel times (Figure 12). The tau method does not utilize our independent p - Δ data and thus it may produce a model that fits the travel times but not the experimental $dT/d\Delta$ curve. By perturbing the individual $\tau(p)$ values within their statistical uncertainties, we obtain a model which matches both the travel time and apparent phase velocity data. The model in Figure 12 has no low-velocity zone because of a lack of compelling evidence for one in the waveform data. A 32 km thick crust was used arbitrarily; a 15 km thick oceanic crust may also be appropriate to represent the model area. The somewhat gradual crust-mantle transition is required by the very slow observed travel times from 9° to 13° (see Figure 10). The gradient above the 400 km transition zone is controlled by one group of lower-quality data points which will be discussed in more detail in a later section. The shape of the extremal bound envelope indicates that the best-determined model depth ranges are from 450 - 625 km and below 700 km. This tau model is the starting point for the trial-and-error waveform inversion using synthetic seismograms.

Waveforms

To make a synthetic seismogram, commonly a series of convolutions are performed in the time domain:

$$y(t)=s(t)*m(t)*a(t)*i(t)$$

where y is the seismogram, s is the source-time function, a is the attenuation operator, i is the instrument response, and m is the Green's function for the travel path (Helmberger & Burdick, 1979). In order to isolate the desired quantity, $m(t)$, estimates of $s(t)$, $a(t)$, and $i(t)$ must be made.

The source-time functions s(t) for events of $m_b \sim 5.5$ are often short (2 - 3 s) and impulsive, especially for subduction zone earthquakes. Thus for many of the events, a clear pulse which bottomed in a smooth portion of the mantle is the first arrival, separated from and followed by the reflected or refracted mantle-generated phase (see Figure 4 for an example). In this case the first arrival represents the source-time function s(t) convolved with the instrument response i(t); this is valid across the entire array. The attenuation operator is neglected; possible problems associated with this are discussed below. By extracting an high-quality first arrival from an actual digital seismogram to use as the source-instrument response, we eliminate source uncertainty from the modeling problem. Of course each event must be modeled with the appropriate source wavelet. Only one convolution is made in the synthetic calculation: mantle response with the source wavelet time series. Only events with simple source-time functions are used in the modeling process.

To compute the mantle Green's functions, the WKBJ method (Chapman, 1976; Wiggins, 1976) is utilized. Formulated for inhomogeneous media, this technique cannot readily accommodate causal attenuation and is not as accurate near first-order discontinuities and for grazing incidence as some other methods. It is, however, very rapid to compute WKBJ seismograms so that a wide suite of models can be tried at little expense. This modeling allows the inclusion of relative amplitude and waveform data which are sensitive to velocity gradients in the mantle. It is used to "fine-tune" the models already derived from travel time and $dT/d\Delta$ data.

We chose a subset of seven simple events to model, covering the distances 13° to 30°. Starting from the tau model derived earlier, relative amplitude and timing problems were identified and corrected. Then the T - Δ and p - Δ plots are generated for the revised model to insure that those parameters remain acceptable. This iterative scheme is continued until all three data types are matched. The model is then simplified as much as is possible while still matching the data. The final model, GCA, is the result of more than 100 iterations using waveforms.

Results

Relative Amplitude Patterns

Model GCA (Figure 13), which incorporates waveform data, differs considerably in detail from the travel-time derived starting model (Figure 12). Relative amplitudes provide constraints which eliminate many models allowed by the travel time and imperfect ray parameter measurements. In our data set, many separate events overlap in distance and are characterized by similar and stable relative amplitude patterns, which we use in the synthetic seismogram modeling.

From 9° to 13°, event signatures are generally complicated and exhibit less consistency array-wide than do the more distant events. The two events in this distance range (nos. 3 and 10 in Table 1) are small, with m_bs of 5.0 and 5.3 respectively. As they are located in the Gulf of California, their mechanisms are probably strike-slip with a P-wave node facing the array; the source characteristics are complex, vary with azimuth and so often result in poor records. While first arrivals are small, no weakening trend with increasing distance or obvious secondary arrivals argue conclusively for the presence of a well-defined low-velocity zone. Travel times are very slow in this distance range, and apparent velocity measurements are scattered and less reliable due to poor signal-to-noise ratios for many records.

Very weak initial arrivals and energetic secondary phases characterize seismograms at distances of 14° to 18° (see Figure 3). At 15°, the secondary arrival, which is the reflection from the 390 km discontinuity, is 6 s behind the first break. Complex interference patterns develop near 18° as the later phase moves through and takes over as the first arrival.

Small near 19°, the first arriving energy increases in amplitude relative to a strong secondary phase until a distance of 21°. Now the initial-arriving energy is bottoming in the smooth portion of the mantle between 400 and 650 km. At this range both wavelets are equal in amplitude; the second wavegroup arrives 3 to 4 s behind the first (Figures 4, 5). The first arrival weakens near 23° and an interference pattern emerges at 24° between the two phases. This amplitude pattern is duplicated for several events in this distance range. The strong later arrival observed here is the part of the EF branch (Figure 10b) of the travel time curve which bottoms at the lower discontinuity. For many u_t per mantle models (e.g. those of King & Calcagnile, 1976; and Burdick & Helmberger, 1978), the AB branch would be moving out in this distance range with large amplitudes and would be highly visible. The null-observation of this travel time branch plays an important role in the modeling process.

From 26° to 28° a secondary arrival moves out and weakens relative to the first arrival (see Figure 6). This is the "back branch" of the second triplication and is part of the CD travel time branch. Seismograms become simple in character at distances beyond 28°.

Model Description

The crust, uppermost mantle and low-velocity zone of GCA (Figure 13, Table 2), while subject to some bounding information, are non-unique. Above 125 km, the model parameters are adjusted mainly to agree with travel times, subject to several constraints: a single layer, 20 km crust is a compromise between the 30-km, two-layer southern California structure and a thin oceanic crust. The Pn velocity is set at 7.9 km/s, the best value for southern California (Hearn, 1983) and assumed to be appropriate for continental areas of northwest Mexico covered by GCA. Travel times beyond 13° control the integral of the size of the

low-velocity zone and the absolute velocities above 125 km.

Arrivals closer than 13.5° are in the shadow zone of GCA (see Figure 10b). An offset in the travel time data is also observed at that distance. Figure 1 shows that the two closest events, in the Gulf of California, have midpoints beneath the Gulf itself, while the events from 13° - 18° (nos. 2,4,12,13 in Table 1) are located on the Rivera Fracture Zone, and their rays turn under the Baja California peninsula. The offset travel times could be due to strong lateral variations between the two regions for depths of less than 150 km. Travel times from only events 3 and 10 (Table 1) and an arbitrary crustal structure were used in a separate tau inversion for shallow structure of the Gulf itself. Figure 14 shows that, in the absence of a low velocity zone that would put 9° - 13° in a shadow zone, the transition from crust to mantle must be gradual for the spreading center (Figure 14, Table 3). A smooth, gradual crust-mantle transition is also documented for the Jordan-Dead Sea rift (Ginzburg et al., 1979). The travel times of Figure 10b, then, can be satisfied by model GCA' (Table 3) for distances of less than 13° and GCA beyond 13.5°. While two models are proposed based on the shift in travel times at 13°, both GCA and GCA' satisfy the waveform data from 13° to 15° reasonably well. These two models are based on the differing crust-mantle transitions between the Gulf of California and adjacent continental areas. While the Gulf itself may have no seismic lid, a gradual crust-mantle transition and no velocity reversal, the continental portion of the study area, with more usual Pn velocities, requires a region of negative velocity gradient to satisfy travel time data.

Tight constraints on the model shape begin at depths of 125 km. The small amplitude first arrivals from 15° to 17° require a very slight positive velocity gradient between 125 and 225 km (see Figure 15). A model for the western United States, T7 of Burdick & Helmberger (1978), has a more moderate

gradient in this distance range and produces large first arrivals at 15° (Figure 15). The first arrivals of GCA are still large relative to the 390-km reflection at these distances, but Q may have an important effect here. The initial arrivals spend more time in the highly-attenuating asthenosphere than do the mantle reflections.

A first-order discontinuity of 4.9% at 390 km produces large amplitude secondary arrivals at 14° which become first arrivals near 18° (see the CD branch of Figure 10b). All discontinuities in GCA are represented as steps in velocity because equivalent gradients over 10 - 20 km are not resolvable. In many regions, the "back branch" of the 390 km travel-time triplication (AB branch) is observed to distances of 24° (England et al., 1977; Burdick & Helmberger, 1978; and others) or even past 30° (King & Calcagnile, 1976). This is indicative of a small velocity gradient between 300 and 400 km which is inefficient at turning energy to the surface so that it is seen at larger ranges. The data used in this study show no evidence for the AB branch past 20° for 9 of 10 events in that distance interval. The anomalous event has a complicated source and a low signal-to-noise ratio, and occurred on a fracture zone rather than in the subduction regime (Figure 16). In the tau inversion, dubious secondary times from that event (no. 26 in Table 1) are used to help define the first discontinuity, so the resulting model has a more modest gradient above 400 km. Synthetic seismograms for this structure, however, fit observations from 20° to 23° very poorly (see Figure 17). The absence of an observed AB branch past 20° thus requires the steep velocity gradient seen in GCA from 225 to 390 km. This unusual gradient is well-supported by the data and is a feature significantly different from models proposed for shields, trenches or tectonic-continental areas.

Large first arrivals are produced from 20° to 23° by the strong velocity gradient from 390 to 620 km depth; a small inflection at 540 km amplifies initial pulses near 21° (Figure 17). The shape of the velocity-depth curve from 620 to 700 km is particularly well-resolved by large amounts of data recorded in the appropriate distance interval, 22° - 28°. Figure 18 shows synthetic seismograms generated for different shapes of the 660 km discontinuity compared to the data. The very fast velocity increase from 620 to 660 km is necessary to generate the correct relative amplitudes between the EF branch (first arrival) and CD branch (second phase) on the seismograms at 25.9° and 27.1°. Improved amplitude and timing relationships at 23° are gained by increasing the gradient just below the discontinuity. Thus a first order velocity jump of only 2.8%, coupled with large gradients immediately above and below, satisfies the waveform data best.

Observed seismograms are simple beyond 28° in distance (Figure 6). The gradient which fits the p - Δ data is adopted in GCA and is very similar to that for a JB earth.

The need for a sharp velocity gradient from 250 to 390 km and the increased resolution of the fine structure of the 660 km velocity break mark the improvements in detail of the waveform-constrained model GCA over the earlier tau-derived model for the same data set. The addition of waveform techniques to traditional array analysis of short-period data are important in elucidating the fine structure of the upper mantle.

Discussion

Many past studies of upper mantle structure have relied on less than high-quality short-period travel time and waveform data, either from discrete receivers or small arrays. The advantages of large-aperture arrays such as SCARLET or NORSAR are obvious: stable $dT/d\Delta$ measurements can be made using the whole network or subsets of it, secondary arrivals with differing phase velocities are easily identifiable, and anomalous traces, such as those contaminated by unusual receiver structure, can be identified and discarded. For suitably simple events, waveform modeling is a useful tool for short-period data as well as the more stable long-period energy. As more high-quality digital data becomes available, additional detailed investigations including many data types should result in less ambiguous, better resolved upper mantle models.

A comparison of the spreading center model GCA with well-constrained models for differing tectonic regimes is very revealing. We consider a continental shield model K8 (Given & Helmberger, 1980), tectonic-continental model T7 (Burdick & Helmberger, 1978), and trench-arc model ARC-TR (Fukao, 1977) (Figure 19). K8, which represents northwest Eurasia, was derived from synthetic seismogram modeling of both long- and short-period P waves and is constrained to fit the NORSAR-determined $p - \Delta$ curve of model KCA (King & Calcagnile, 1976). Similarly, Burdick & Helmberger's (1978) western United States model T7 relies on the Johnson (1967) apparent velocity measurements (made at TFSO in Arizona) as well as waveform modeling of earthquakes with known source mechanisms. An unusually complete travel time and $dT/d\Delta$ data set constrain the parameters of ARC-TR, a model for the Pacific Ocean trench near Japan. Figure 19 shows that all four velocity-depth curves are quite similar below 400 km depth, with some slight differences in velocity gradient at depths greater than 670 km. The small disparities in the depths to the "400 km" and "670 km"

discontinuities are probably not resolvable within the data constraints and modeling error.

For depths shallower than 400 km, however, significant differences between the regions appear. In all the models, lid and low-velocity zone shapes are non-unique, with the arc and shield models predicting considerably faster arrival times for regional distances than do the young continent and ridge representations. At about 200 km, K8, T7 and ARC-TR converge, while GCA features much lower velocities. Low (ARC-TR) to moderate (K8, T7) velocity gradients prevail between 200 km and 400 km except for GCA, in which velocity increases very rapidly with depth in that depth range; GCA velocities merge with the other models at 350 km.

Low velocities for both P and S waves are well-documented for oceanic ridges and continental rifts. Surface wave dispersion studies require very low S-wave speeds beneath young ocean (e.g. Knopoff et al., 1970; Montagner & Jobert, 1981; Wielandt & Knopoff, 1982). Detailed refraction work performed on rifts (Ginzburg et al., 1979; Maguire & Long, 1976; Puzyrev et al., 1973) supports low values for Pn velocities. Oceanic ridge refraction studies (e.g. Gettrust et al, 1982; Lewis & Garmany, 1982) find compressional speeds of 8.0 km/s at shallow (8 km) levels, but this "lid" may be very thin (see Bulin, 1979) and underlain by extremely slow material.

There is little data pertinent to the deep structure of rifts and ridges. Available P-residuals (Rowlett & Forsyth, 1978) and PP-residuals (Dorbath & Dorbath, 1981) for the Mid-Atlantic Ridge are large and positive, indicating very low velocities, possibly to great depth. Very late P-wave arrivals at Addis-Ababa (Dziewonski & Anderson, 1983) are also observed for the East African Rift. Thus the velocity value of only slightly over 8 km/s at 200 km in GCA is consistent with the available data.

Small observed first arrival amplitudes from 14° - 16° require a very slowly increasing velocity from 100 to 200 km. The gradient, however, trades off with a possible low Q zone just below the lid which could reduce the amplitudes of the first arrivals near 14°. While such an attenuating zone will probably have a greater effect on wave amplitudes than on periods, the synthetic seismograms indicate that there is no noticeable frequency depletion of the first arrival relative to the second at 14°.

The main reason for GCA's steep gradient from 225 - 390 km is that no arrivals corresponding to the AB travel time branch (Figure 10b) are observed beyond a (surface focus) distance of 20°. In some shield regions (King & Calcagnile, 1976), this branch is noted past 30°. Typical observational limits for tectonic continental areas are 24° to 26° (Wiggins & Helmberger, 1973; Ram et al., 1977; Burdick & Helmberger, 1978). England et al. (1978) used oceanic events recorded at NORSAR for their model NAT and see the AB branch to 24°, but for that range the rays' bottoming points are no longer beneath young ocean, so a different structure might be expected. In Australia, Simpson et al. (1974) do not observe an AB branch beyond 21°. Model SMAK I has a small velocity gradient above 400 km which predicts AB arrivals well past 30°; Simpson et al. appeal to a properly placed low Q zone to suppress amplitudes of the AB phase. For Indian Ocean earthquakes recorded at the Gauribidanur array in southern India, Ram & Mereu (1977) cannot identify the AB branch past 19°. Their model RM-3 also has a shallow gradient above 400 km but terminates the AB branch with a very deep (175 - 332 km) low velocity zone.

Other studies with oceanic sources, therefore, document the absence of the AB branch beyond 20° but resort to non-deterministic methods to diminish that phase's amplitudes. Since low upper mantle velocities are consistent for ridges, the very slow uppermost mantle of GCA underlain by a region of unusually fast

velocity increase with depth is very appropriate and a less artificial way of effectively shortening the predicted AB travel time branch.

Shear wave data from the East Pacific Rise support the idea of a large velocity gradient between the depths of 200 and 400 km. Grand & Helmberger's (1983) model TNA (Figure 20), derived from long-period SS phases recorded at North American stations, is very similar to GCA in general character, and includes a high gradient from 250 - 400 km in depth.

The discontinuities near 400 km in the four models of Figure 19 are all quite consistent in size and shape. The absolute depth to the velocity transition is dependent on the assumed shallow structure, so the slightly deeper discontinuity of K8 is probably not significant. The Fukao (1977) model ARC-TR has a pronounced "bump" in the velocity-depth profile at 500 km because of a rapid decrease in $p(\Delta)$ at 20°. GCA also has a very slight inflection near 540 km to match strengthened first arrival amplitudes near 21°. While all the models are very similar in the 650 km depth range, GCA is derived from the most complete data set in the 20° - 30° interval. The seismograms shown in Figures 4, 5, 6 are very sensitive to the fine structure of the 660 km discontinuity as is demonstrated in Figure 18. The T7 model contains the strong gradient just above 670 km but a lack of convincing data near 27° precludes delineation of the transition shape just below the break. Grand & Helmberger (1983) include increased gradients from 660 km to 750 km for both shield and tectonic S-wave models, while a P-wave model for a shield has a similar form (Given & Helmberger, 1980). Dziewonski & Anderson's (1981) model PREM also features an increased gradient near 700 km on a global scale.

The differences between the four models with depth are further illustrated by comparison of cumulative one-way vertical travel times. In Figure 21, vertical travel times are computed for each model starting at 620 km in 20 km steps and

are compared to the Herrin (1968) velocity model. It is evident that the curves for T7 and GCA are very similar from 620 km to 300 km, then T7 flattens out with respect to the Herrin times while GCA continues to be very slow relative to the 1968 model. ARC-TR and K8 also have nearly constant values for $T-T_{Herrin}$ for 100 - 200 km depth. The arc and shield models' residuals decrease above 150 km as expected from their faster uppermost mantle velocities, while T7 and GCA become more positive for that depth range. The various crustal thicknesses have large effects on the overall vertical travel times.

Conclusions

Earthquakes in Mexico recorded at SCARLET form a unique, high-density digital short-period P-wave data set for upper mantle study. We have analyzed over 1400 seismograms and utilized travel time, apparent phase velocity and relative amplitude information to produce a tightly constrained, detailed model for depths to 1000 km beneath an active oceanic ridge region, the Gulf of California. Unusually low velocities to depths of 350 km characterize the spreading center model, consistent with teleseismic P and PP residuals of Rowlett & Forsyth (1979) and Dorbath & Dorbath (1981), respectively. The abrupt cutoff in distance of observations of the travel time branch (AB) for which rays bottom just above 400 km leads to an interpretation of an anomalously high velocity gradient from 225 to 390 km, rather than a large velocity step at the base of the low velocity zone. Grand & Helmberger (1983) make a similar observation for shear waves from East Pacific Rise earthquakes. Thus the ridge model, GCA, differs significantly from models observed for shield, young continental, and arc regimes to 350 km depth.

Abundant data from 19° to 28° constrain the detailed shape of the 660 km discontinuity. A small, 2.8% jump in compressional velocity is accompanied by

increased gradients both above and below the break.

Present available data are not sufficient to confirm or reject the idea of undulations of the major velocity discontinuities in the upper mantle. Lateral velocity variations between shields, arcs, and tectonic-continental regions seem well established to depths of 200 km. This study demonstrates that oceanic spreading centers have velocities slower than the other regions to the even greater depth of 350 km.

Acknowledgments

The author thanks D.L. Anderson, R. W. Clayton, D. V. Helmberger and J. W. Given for ideas and advice related to this project. J. Given wrote the WKBJ program, and L. R. Johnson provided the tau inversion code. D. Anderson, R. Clayton and H. Kanamori reviewed the manuscript and suggested improvements. This work was supported by National Science Foundation grant EAR-811-5236, NASA contract NSG-7610 and U. S. Geological Survey contract 14-08-0001-19720. Contribution no. 3887, Division of Geological and Planetary Sciences, California Insitute of Technology, Pasadena, CA, 91125, USA.

References

Bessonova, E. N., Fishman, V. M., Ryaboyi, V. Z., & Sitnikova, G. A., 1974. The tau method for inversion of travel times - I. Deep Seismic Sounding Data, *Geophys. J. R. astr. Soc.*, **36**, 377-398.

Bessonova, E. N., Fishman, V. M., Shnirman, M. G., Sitnikova, G. A. & Johnson, L. R., 1976. The tau method for inversion of travel times - II. Earthquake Data, *Geophys. J. R. astr. Soc.*, **46**, 87-108.

Bulin, N. K., 1979. Upper mantle velocities on the northern Cocos plate - A Discussion, *Earth Planet. Sci. Lett.*, **43**, 168-171.

Burdick, L. J. & Helmberger, D. V., 1978. The upper mantle P velocity structure of the western United States, *Jour. Geophys. Res.*, **83**, 1699-1712.

Chapman, C. H., 1976. A first-motion alternative to geometrical ray theory, *Geophys. Res. Lett.*, **3**, 153-156.

Dey-Sarkar, S. K. & Wiggins, R. A., 1976. Upper mantle structure in western Canada, *Jour. Geophys. Res.*, **81**, 3619-3632.

Dorbath, C. & Dorbath, L., 1981. Travel time residuals of PP waves reflected under the central Atlantic Ocean, *Phys. Earth Planet. Int.*, **25**, 121-128.

Dziewonski, A. M. & Anderson, D. L., 1981. Preliminary reference earth model, *Phys. Earth Planet. Int.*, **25**, 297-356.

Dziewonski, A. M. & Anderson, D. L., 1983. Travel times and station corrections for P-waves at teleseismic distances, in press, Journal of Geophysical Research.

England, P. C., Worthington, M. H., & King, D. W., 1977. Lateral variation in the structure of the upper mantle beneath Eurasia, *Geophys. J. R. astr. Soc.*, **48**, 71-79.

England, P. C., Kennett, B. L. N., & Worthington, M. H., 1978. A comparison of upper-mantle structure beneath Eurasia and the North Atlantic and Arctic

Oceans, *Geophys J. R. astr. Soc.*, **54**, 575-585.

Fukao, Y., 1977. Upper mantle P structure on the ocean side of the Japan-Kurile arc, *Geophys. J. R. astr. Soc.*, **50**, 621-642.

Gettrust, J. F., Furukawa, K. & Kempner, W. G., 1982. Variation in young oceanic crust and upper mantle structure, *Jour. Geophys. Res.*, **87**, 8435-8446.

Ginzburg, A., Makris, J., Fuchs, K., Perathoner, B., & Prodehl, C., 1979. Detailed structure of the crust and upper mantle along the Jordan - Dead Sea Rift, *Jour. Geophys. Res.*, **84**, 5605-5612.

Given, J. W. & Helmberger, D. V., 1980. Upper mantle structure of northwestern Eurasia, *Jour. Geophys. Res.*, **85**, 7183-7194.

Grand, S. P. & Helmberger, D. V., 1983. Upper mantle shear velocity structure of North America, submitted to Geophysical Journal of the Royal astronmical Society.

Green, A. G., 1978. An upper mantle P-wave velocity model for eastern and southern Africa, *Pure Appl. Geophys.*, **116**, 1262-1273.

Hadley, D.M. & Kanamori, H., 1977. Seismic structure of the Transverse Ranges, California, *Geol. Soc. Am. Bull.*, **88**, 1469-1478.

Hager, B. H. & Raefsky, A., 1981. Deformation of seismic discontinuities and the scale of mantle convection (abstract), *EOS*, **62**, 1074.

Hales, A. L., 1972. The travel times of P seismic waves and their relevance to the upper mantle velocity distribution, *Tectonophysics*, **13**, 447-482.

Hearn, T. M., 1983. Pn travel times in southern California, submitted to Journal of Geophysical Research.

Helmberger, D. V. & Wiggins, R. A., 1971. Upper mantle structure of the midwestern United States, *Jour. Geophys. Res.*, **76**, 3229-3245.

Helmberger, D. V. & Burdick, L. J., 1979. Synthetic seismograms, *Ann. Rev. Earth Planet. Sci.*, **7**, 417-442.

Herrin, E., 1968. 1968 seismological tables for P phases, *Bull. Seis. Soc. Am.*, **58**, 1193-1241.

Lamanuzzi, V. D., 1981. Relative Pn travel-time residuals for stations in southern California. M. S. Thesis, University of Southern California, Los Angeles, 117pp.

Johnson. C. E., 1979. I: CEDAR - An approach to the computer automation of short-period seismic networks, II: Seismotectonics of the Imperial Valley of southern California, Ph. D. Thesis, California Institute of Technology, Pasadena, 332pp.

Johnson, L. R., 1967. Array measurements of P velocities in the upper mantle, *Jour. Geophys. Res.*, **72**, 6309-6325.

Kanamori, H. ,1967. Upper mantle structure from apparent velocities of P waves recorded at Wakayama Micro-Earthquake Observatory, *Bull. Earthq. Res. Inst.*, **45**, 657-678.

Kanamori, H. & Hadley, D. M., 1975. Crustal structure and temporal velocity change in southern California, *Pure Appl. Geophys.*, **113**, 257-28

King, D. W., & Calcagnile, G., 1976. P-wave velocities in the upper mantle beneath Fennoscandia and western Russia, *Geophys. J. R. astr. Soc.*, **46**, 407-432.

Knopoff, L., Schlue, J. W., & Schwab, F. A., 1970. Phase velocities of Rayleigh waves across the East Pacific Rise, *Tectonophysics*, **10**, 321-334.

Lenartowicz, E., & Albert, R. N. H., 1980. P-wave travel-time residuals and the crust and upper mantle lateral inhomogeneities in Africa, *Tectonophysics*, **67**, 123-137.

Lewis, B. T. R. & Garmany, J. D., 1982. Constraints on the structure of the East Pacific Rise from seismic refraction data, *Jour. Geophys. Res.*, **87**, 8417 8425.

McMechan, G., 1979. An amplitude constrained P-wave velocity profile for the upper mantle beneath the eastern United States, *Bull. Seism. Soc. Am.*, **69**, 1733-1744.

Maguire, P. K. H. & Long, R. E., 1976. The structure on the western flank of the Gregory Rift (Kenya) Part I. The Crust, *Geophys. J. R. astr. Soc.*, **44**, 661-675.

Manchee, E. B. & Weichert, D. H., 1968. Epicentral uncertainties and detection probabilities from the Yellowknife seismic array data, *Bull. Seism. Soc. Am.*, **58**, 1359-1377.

Massé, R. P., 1973. Compressional velocity distribution beneath central and eastern North America, *Bull. Seism. Soc. Am.*, **63**, 911-935.

Massé, R. P., 1974. Compressinal velocity distribution beneath central and eastern North America in the depth range 450 - 800 km, *Geophys. J. R. astr. Soc.*, **36**, 705-716.

Montagner, J. P. & Jobert, N., 1981. Investigation of upper mantle structure under young regions of the southeast Pacific using long-period Rayleigh waves, *Phys. Earth Planet. Int.*, **27**, 206-222.

Nolet, G. & Mueller, S., 1982. A model for the deep structure of the east African rift system from simultaneous inversion of teleseismic data, *Tectonophysics*, **84**, 151-178.

Okal, E. A. & Anderson, D. L., 1975. A study of lateral heterogeneities in the upper mantle by multiple ScS travel-time residuals, *Geophys. Res. Lett.*, **2**, 313-316.

Puzyrev, N. N., Mandelbaum, M. M., Krylov, S. V., Mishenkin, B. P., Krupskaya, G. V. & Petrich, G. V., 1973. Deep seismic investigations in the Baikal rift zone, *Tectonophysics*, **20**, 85-95.

Raikes, S. A., 1980. Regional variations in upper mantle structure beneath southern California, *Geophys. J. R. astr. Soc.*, **63**, 187-216.

Raikes, S. A. & Hadley, D. M., 1979. The azimuthal variation of teleseismic P-residuals in southern California: Implications for upper-mantle structure, *Tectonophysics*, **56**, 89-96.

Ram, A. & Mereu, R. F., 1977. Lateral variations in upper mantle structure around India as obtained from Gauribidanur seismic array data, *Geophys. J. R. astr. Soc.*, **49**, 87-113.

Ram, A., Mereu, R. F., & Weichert, D. H., 1978. Ther identification and interpretation of upper mantle travel-time branches from measurements of $dT/d\Delta$ made on data recorded at the Yellowknife seismic array, *Can. J. Earth Sci.*, **15**, 227-236.

Rowlett, H. & Forsyth, D., 1979. Teleseismic P-wave delay times in a major oceanic fracture zone, *Geophys. Res. Lett.*, **6**, 273-276.

Sipkin, S. A. & Jordan, T. H., 1975. Lateral heterogeneity of the upper mantle determined from the travel times of ScS, *Jour. Geophys. Res.*, **80**, 1474-1484.

Sipkin, S. A. & Jordan, T. H., 1976. Multiple ScS travel times in the western Pacific: implications for mantle heterogeneity, *Jour. Geophys. Res.*, **81**, 853-861.

Simpson, D. W., Mereu ,R. F. & King, D. W., 1974. An array study of P-wave velocities in the upper mantle transition zone beneath northeastern Australia, *Bull. Seism. Soc. Am.*, **64**, 1757-1788.

Walck, M. C. & Minster, J. B., 1982. Relative array analysis of upper mantle lateral velocity variations in southern California, *Jour. Geophys. Res.*, **87**, 1757-1772.

Wielandt, E. & Knopoff, L., 1982. Dispersion of very long-period Rayleigh waves along the East Pacific Rise: Evidence for S wave velocity anomalies to 450 km depth, *Jour. Geophys. Res.*, **87**, 8631-8641.

Wiggins, R. A., 1976. Body-wave amplitude calculations - 2, *Geophys. J. R. astr. Soc.*, **46**, 1-10.

Wiggins, R. A. & Helmberger, D. V., 1973. Upper mantle structure of the western United States, *Jour. Geophys. Res.*, **78**, 1870-1880.

Figure Captions

(1) Location map for this study. Stars are epicenters of the 22 earthquakes closer than 30°. Small (2°) portions of the great circles between SCARLET and the events are also shown, indicating the area covered by model GCA. Note that all the arc segments fall within the region affected by the Gulf's spreading. Circles locate the calibration events which are farther than 30° from Pasadena.

(2) Stations of the southern Califonia array used in this paper. Empirical corrections for these 98 stations are shown in Figure 9. Latitude is in degrees north, longitude in degrees west.

(3) An example of an event record section recorded at SCARLET along with the synthetic section predicted by model GCA. Distances are not corrected for event depth. Amplitudes are scaled to the maximum of each trace. Empirical station corrections (Figure 9) have been applied, and the data have been filtered with a bandpass of .01 to 5 Hz. For clarity, only a few representative seismograms are shown. a) A shallow event on the Rivera Fracture Zone (no. 2 in Table 1) which shows a weak first arrival followed by the reflection from the 390 km discontinuity. b) Synthetic section for the same event.

(4) a) A 96 km deep event inland from the Middle America Trench, no. 14 in Table 1. Note the increasing strength of the first arrival near 20° and the strong arrival from the 660 km discontinuity. Also the "back branch" of the 390 km triplication (see Figure 10b) is not in evidence. See Figure 3 for format explanation. b) Synthetic section for event 14 using GCA. c) Synthetic section for the same event for model T7 (Burdick & Helmberger, 1978). Note the strong AB branch extending to 22°, which is not visible in the data.

(5) a) Format is the same as Figure 3. No. 17 of Table 1 is 56 km deep. Again a strong first arrival and reflection from the 660 km velocity discontinuity are visible with no sign of the AB travel time branch past 20°. b) GCA synthetic section for event 17. c) T7 synthetic section for event 17. Again the AB branch is a very strong phase in these synthetic seismograms, but not observed in the data.

(6) a) No. 27 (Table 1), in the same format as Figure 3. Here the "back branch" of the 660 km triplication moves out with increasing distance, and the relative amplitudes change from a weak first arrival near 26° to a simple pulse near 28°. The coherent energy at 109 seconds is pP of this 80 km deep earthquake. b) GCA synthetic section for event 27.

(7) a) Data record section of 10 events spanning 9° to 40°. Amplitudes and filtering are as in Figure 3. Station and depth corrections have been applied. The mantle triplication phases are clearly visible. b) Synthetic record section for GCA on the same scale, computed for surface focus. Source wavelets vary with distance.

(8) Comparison of event 20 (Table 1) before and after application of empirical station corrections. Record sections are set up as in Figure 3. a) uncorrected. b) corrected. Note the improved alignment of the traces near 30.3°,31.9°,33.1°, and 34.4°.

(9) A comparison between the teleseismic P residuals of Raikes (1980) and the empirical station corrections used in this study. Raikes' values (b) are referenced to station GSC and include corrections for elevation, sediments and crustal thickness which are not included in (a). Still many similarities exist, such as relatively negative values near (35°,-118°), positive residuals at (34.5°,-116.5°), negative (fast) corrections in the Santa Barbara Channel (34°,-120°) and negative values southeast of the Imperial Valley (33°,

-115°). Differences occur due to elevation, sediment cover and crustal thickness in the Peninsular Ranges (33°,-116°) and the Ventura Basin (34.5°, -119°). The contour interval is 0.2 s.

(10) Travel time data for the 29 events. a) Travel times vs distance, reduced by 10 km/s and corrected for elevation, depth and receiver structure. Data coverage is almost continuous from 9°-40°. There are 1753 data points; 438 are secondary arrivals. b) Models GCA and GCA' superimposed on the baseline-shifted travel times. GCA' is constructed for the axial region of the Gulf of California from only very close (9°-13°) data, while GCA represents adjacent continental areas; it has a thin lid and small low-velocity zone. The two models merge below 150 km. Data near (22°, 60 s) correspond to the anomalous p - Δ point of Figure 11. Letters refer to travel time branches discussed in the text.

(11) The 58 p - Δ points plotted with GCA. Triangles indicate measurements made with first arrivals; circles are secondary phases. The data point at 12.0,s/°, 23° is from event 26 and is discussed in the text.

(12) The results of tau inversion of the travel times shown in Figure 10. The solid line is the inversion of the best tau values, while the dotted lines represent error bounds implied by error estimates for each tau point. The single inversion model is used as the starting model for forward computations of synthetic seismograms.

(13) Model GCA. Valid for the Gulf of California spreading region, GCA features a 20 km crust and low velocities to 350 km depth, with an unusually large velocity gradient from 225 to 390 km. Velocity discontinuities are 4.9% at 390 km and 2.8% at 660 km.

(14) The top 150 km of GCA compared with GCA', the model constructed by tau inversion of arrival times from earthquakes closer than 13°. GCA' has no low velocity zone and a transition zone at the crust-mantle boundary. The difference between these models may represent lateral crustal variations between the Gulf of California itself (GCA') and the adjacent continental areas.

(15) A comparison of waveform data for distances of 14° - 18° with various models. The top row is the data, followed by GCA, the tau starting model and T7 (Burdick & Helmberger, 1978). Distances are corrected for depth. All seismograms are from event 2 (Table 1) and are scaled and filtered as in Figure 3. At Δ = 14.7° and 15.2°, the tau and T7 models predict a first arrival much stronger than the 390 km reflection., while GCA comes closer to the true relative amplitudes. The models are very similar at 16.3° and 17.6°.

(16) Record section for event 26 (Table 1), reduced by 11 km/s. The line indicates the arrivals picked as the AB branch in Figure 7 and used in the tau inversion. Notice the poor signal coherency and signal-to-noise ratio compared to the sections in Figures 3, 4, 5, and 6.

(17) Same as Figure 15 for 20° to 23°. All data are from event 14 (Table 1) except for the trace at 21.7° which is from event 17. At 20.3°, GCA correctly predicts times and amplitudes of the two arrivals. The tau model and T7 both have large intermediate arrivals which are from rays turning just above the 390 km discontinuity. The three arrivals in the T7 synthetic are clearly not in the data. At 20.9°, the AB branch arrival is interfering with the reflection from the 660 km velocity jump in T7 and the tau model, causing the relative amplitudes and timing to be off. All three models predict the data at 21.9° rather poorly , but again for the tau and T7 models

the large phase is that of the AB branch. At 22.3° and 23.1°, GCA provides the best fit in terms of subtle timing and amplitude comparisons. Here the AB arrivals would be more than 8 s behind the first break.

(18) Detailed analysis of the 660 km discontinuity. The synthetics are calculated for model GCA with differing gradients above and below 660 km, from a simple step (top row) to large gradients both above and below (bottom row). The relative amplitudes and timing of arrivals are much better for the bottom model than for the other two attempts. Distances are corrected for surface focus.

(19) Four models for differing tectonic regimes. T7 (Burdick & Helmberger, 1978) is valid for a tectonically active continental region. Island arcs are represented by ARC-TR (Fukao, 1977) and shields by K8 (Given & Helmberger, 1980). GCA (this study) represents an oceanic spreading center. K8, T7 and ARC-TR are very similar below 200 km depth, but GCA is substantially slower than the other models to depth of 350 km.

(20) A comparison of TNA, Grand and Helmberger's (1983) shear-wave model for Mexico and the western United States, and GCA. Note the great similarity in general character between the models. TNA has a 4.7% velocity jump at 405 km and a 7.8% change at 660 km.

(21) For a starting depth of 620 km, cumulative vertical one-way travel times are computed for four models and compared to the 1968 Herrin mantle velocities. Symbols are plotted at 20 km intervals. T7 and GCA are very close from 600 km to 320 km, then T7's residuals flatten out but GCA's become increasingly positive. This illustrates the very slow GCA velocities above 350 km.

Tables

(1) The epicentral data are taken from the PDE Monthly Listings of the U. S. Geological Survey. For the $dT/d\Delta$ data, F denotes first arrivals, while L means later-arriving phases. The $dT/d\Delta$ determination for event 10 is unreliable and was discarded. The listed error estimate is that of the least-squares plane fit to the travel times. Arrival data are used only for the 96 stations which have empirical receiver corrections.

(2) Velocity model GCA.

(3) Velocity model GCA'. This model, which merges with GCA below 150 km, is valid along the axis of the Gulf of California.

Table1

EVENT DATA

Event		Date		Epicentral Information: Origin Time			Latitude	Longitude	Depth	Magnitude	dT/dΔ Data: Δ	p	RMS	Arrival	Number of
Number	Day	Mo.	Year	Hr.	Min.	Sec.	degrees	degrees	km	m_b	degrees	s/°	Error, s	Type	Stations
1	26	Feb.	1979	20	10	20.2	17 35.40	-101 8.30	64.	5.1	21.22	10.76	.106	F	9
											22.66	10.33	.103	F	11
											21.85	9.63	.192	L	21
2	21	Sep.	1977	13	15	5	20 01.96	-109 9.24	33.	5.7	15.75	13.32	.350	F	35
											18.63	11.13	.191	L	26
3	10	Dec.	1978	06	39	55.1	6.42	-109 36.56	15.	5.3	9.79	14.44	.379	F	16
											11.65	13.56	.315	F	14
4	25	Oct.	1978	11	35	27.1	17 56.36	-106 20.76	33.	5.2	17.25	12.60	.240	F	22
											19.06	10.50	.157	F	11
5	25	Jan.	1979	10	04	33.0	17 24.76	-100 52.62	41.	5.5	21.35	10.66	.252	F	33
											23.15	10.26	.264	F	16
6	29	Nov.	1978	20	49	46.6	16 11.10	-96 37.80	22.	5.7	24.40	9.22	.092	F	23
											26.23	9.11	.064	F	26
											25.34	10.02	.170	L	49
7	25	Dec.	1978	23	37	55.0	10 21.96	-103 51.90	10.	5.6	25.63	9.00	.372	F	35
8	19	Mar.	1978	01	39	14.0	17 01.56	-99 44.10	26.	5.6	21.94	10.44	.150	F	22
											23.44	9.95	.293	F	26
											22.40	9.36	.277	L	32
9	22	Jan.	1979	06	30	54.3	17 0.00	-94 36.34	107.	5.3	25.35	9.12	.092	F	41
											27.23	9.03	.084	F	21
10	30	May	1978	11	25	41.0	24 48.42	-109 03.36	10.	5.0					
11	10	Sep.	1978	23	24	15.6	14 16.20	-91 29.82	24.	5.6	30.68	6.90	.031	F	65
12	11	Jan.	1978	20	05	24.2	18 46.24	-107 06.40	33.	5.4	16.77	12.61	.193	F	14
											18.75	11.66	.257	F	6
13	18	Dec.	1978	07	59	19.6	19 36.42	-106 56.56	33.	5.2	15.96	13.46	.220	F	20
											18.65	11.32	.265	L	30
14	29	Sep.	1978	16	21	41.0	18 36.90	-102 15.72	95.	5.5	20.56	10.75	.201	F	37
											22.34	10.54	.149	F	15
											20.79	9.46	.332	L	57
15	22	Feb.	1979	09	19	37.0	19 56.60	-100 16.06	56.	5.3	20.10	10.60	.166	F	31
											21.61	10.63	.107	F	11
16	06	Jan.	1979	11	51	30.7	18 16.20	-102 47.10	38.	5.2	19.62	10.97	.333	F	21
											21.73	10.24	.267	F	10
											20.35	9.43	.423	L	34
17	05	Jul.	1978	20	15	18.3	18 29.22	-100 0.42	62.	5.5	21.29	10.46	.129	F	34
											23.21	10.03	.175	F	14
											21.90	9.63	.214	L	45
18	23	Aug.	1978	00	38	32.2	10 12.24	-85 13.32	66.	5.7	37.91	5.42	.046	F	77
19	27	Oct.	1978	14	35	57.3	13 49.98	-90 52.56	66.	5.7	31.44	6.85	.039	F	76
20	06	Dec.	1978	11	52	34.0	13 08.70	-89 36.10	33.	5.6	32.59	6.79	.035	F	77
21	27	Oct.	1978	21	43	24.9	13 46.86	-90 43.80	65.	5.6	31.57	6.85	.039	F	74
22	31	May	1978	01	07	22.4	12 46.02	-87 09.42	75.	5.4	34.59	6.66	.035	F	52
23	06	Dec.	1978	14	26	52.3	13 42.76	-92 17.26	32.	5.7	30.44	6.86	.040	F	71
24	14	Mar.	1979	12	01	24.6	17 57.12	-101 16.96	52.	5.5	20.60	10.65	.163	F	34
											22.43	10.40	.157	F	22
											21.26	9.44	.332	L	50
25	16	Mar.	1979	20	12	31.7	17 32.76	-100 59.46	33.	5.4	20.69	10.72	.135	F	20
											22.45	10.42	.153	F	17

EVENT DATA

Event	Date			Epicentral Information: Origin Time			Latitude	Longitude	Depth	Magnitude	dT/dΔ Data: Δ	p	RMS	Arrival	Number of
Number	Day	Mo.	Year	Hr.	Min.	Sec.	degrees	degrees	km	m_b	degrees	s/°	Error, s	Type	Stations
											21.63	9.49	.249	L	36
86	22	Oct.	1978	14	07	0.8	15 10.56	-104 26.86	33.	5.2	21.26	10.61	.244	P	25
											23.18	10.03	.266	P	19
											22.04	9.49	.510	L	34
											21.35	12.06	.332	L	25
87	4	Jun.	1979	06	26	42.7	15 41.04	-33 35.76	80.	5.7	26.23	9.00	.063	P	61
											27.02	9.01	.225	L	16
88	10	Jan.	1979	13	24	14.3	18 56.64	-93 32.58	156.	5.5	26.01	9.00	.054	P	45
89	26	Jan.	1979	17	10	44.1	17 33.24	-100 59.26	39.	5.4	20.96	10.71	.152	P	16
											22.67	10.46	.147	P	15
											21.79	9.55	.167	L	29

Table 2

Model GCA

Depth	Velocity	Depth	Velocity
km	km/s	km	km/s
0.	6.400	300.	8.403
19.	6.400	325.	8.520
20.	7.900	350.	8.638
35.	7.750	375.	8.750
50.	7.700	390.	8.819
75.	7.850	391.	9.250
100.	7.900	450.	9.476
125.	7.938	538.	9.800
150.	7.975	620.	10.060
175.	8.013	660.	10.360
200.	8.050	661.	10.650
225.	8.100	680.	10.760
250.	8.168	970.	11.340
275.	8.285		

Table 3

Model GCA'

Depth	Velocity
km	km/s
0.0	6.200
5.0	6.400
12.0	6.700
25.5	7.000
31.0	7.500
51.0	7.750
100.0	7.870
115.0	7.970
150.0	8.000

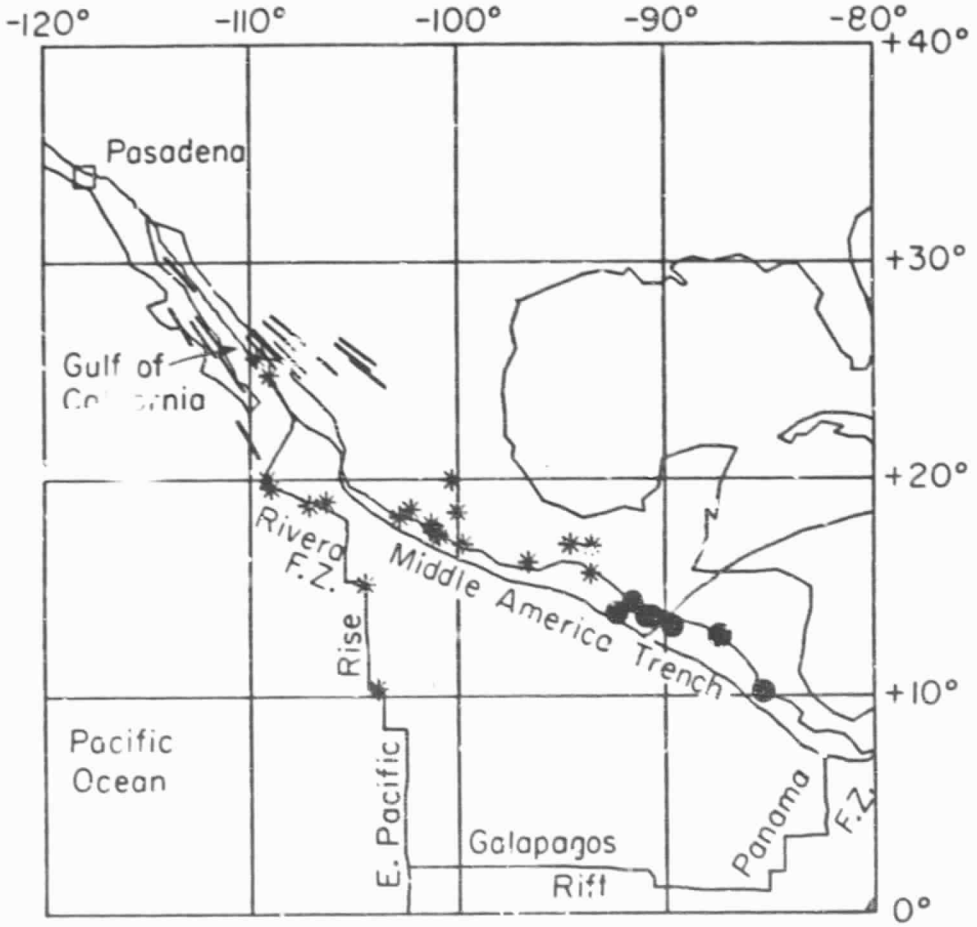

Fig. 1

ORIGINAL PAGE IS
OF POOR QUALITY

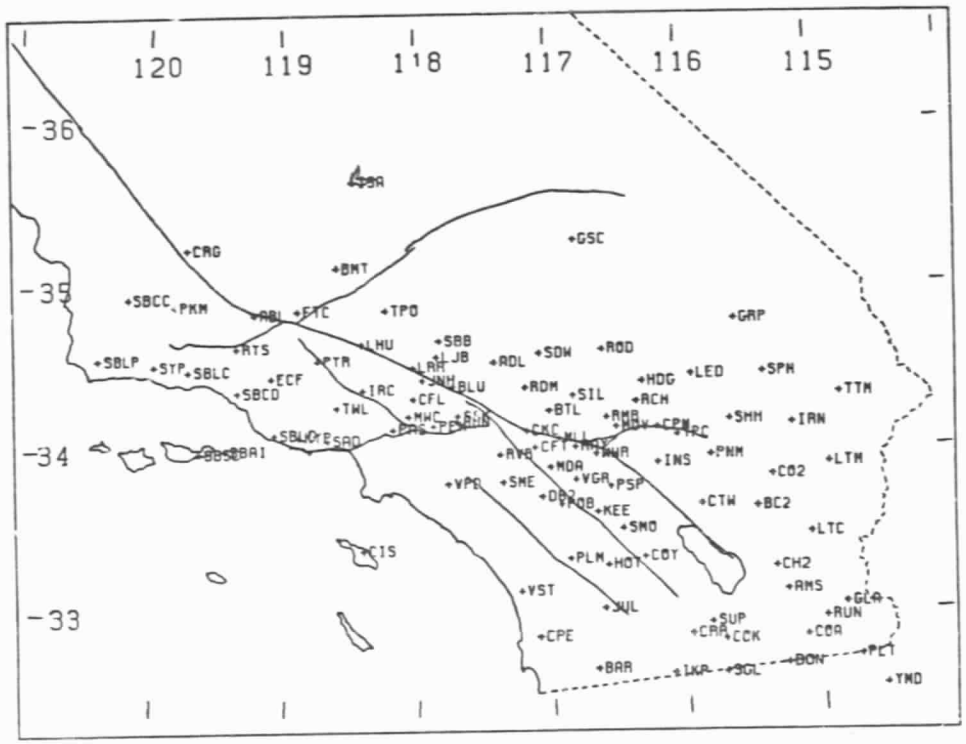

Fig. 2

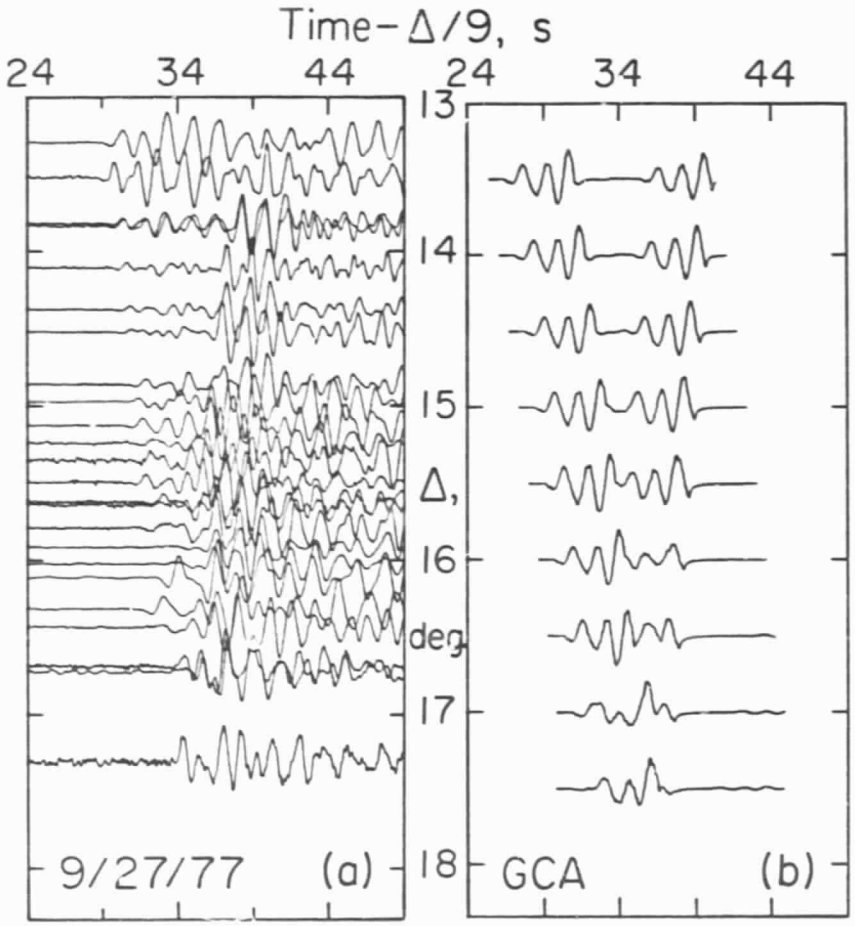

Fig. 3

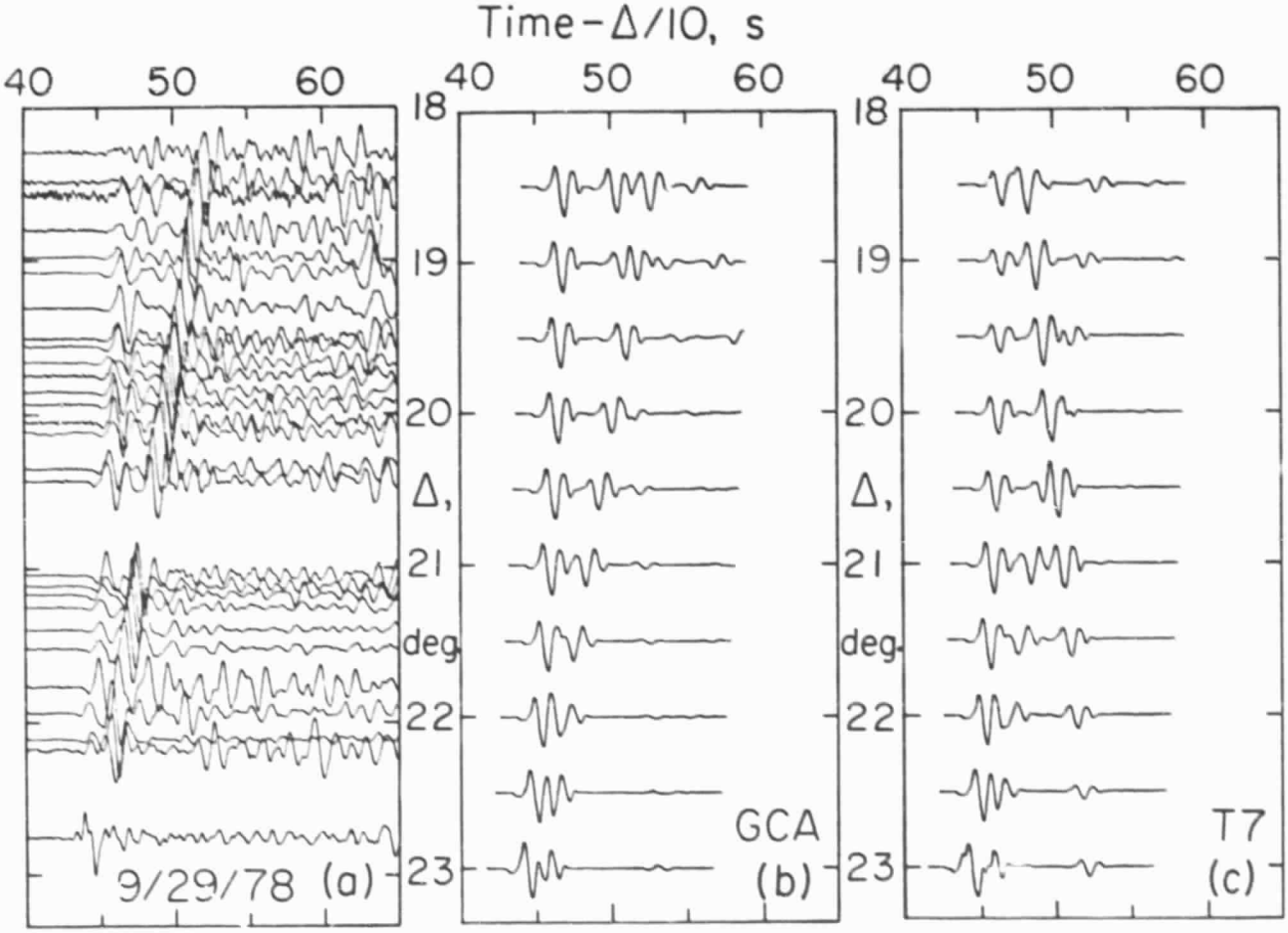

Fig. 4

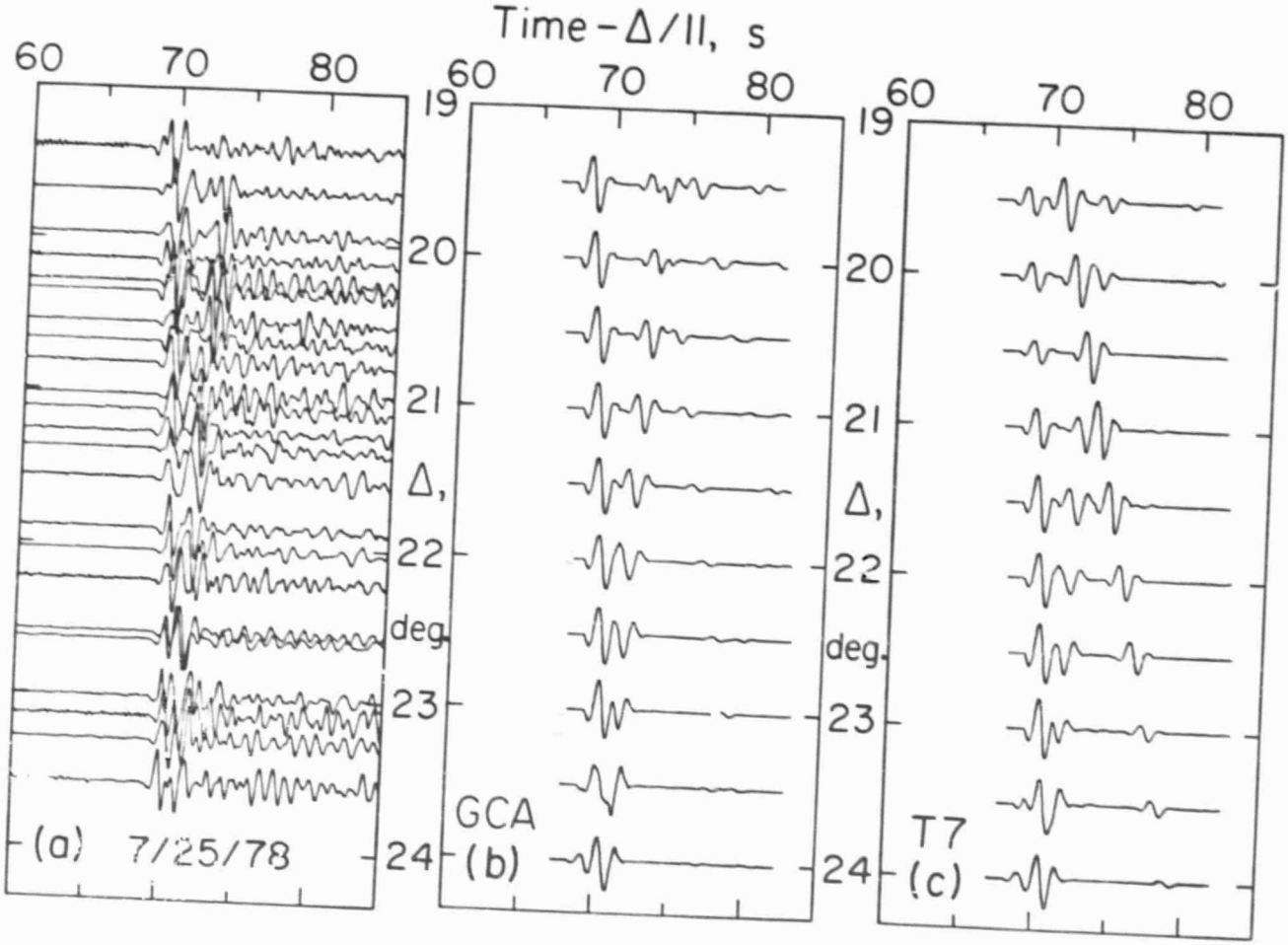

Fig. 5

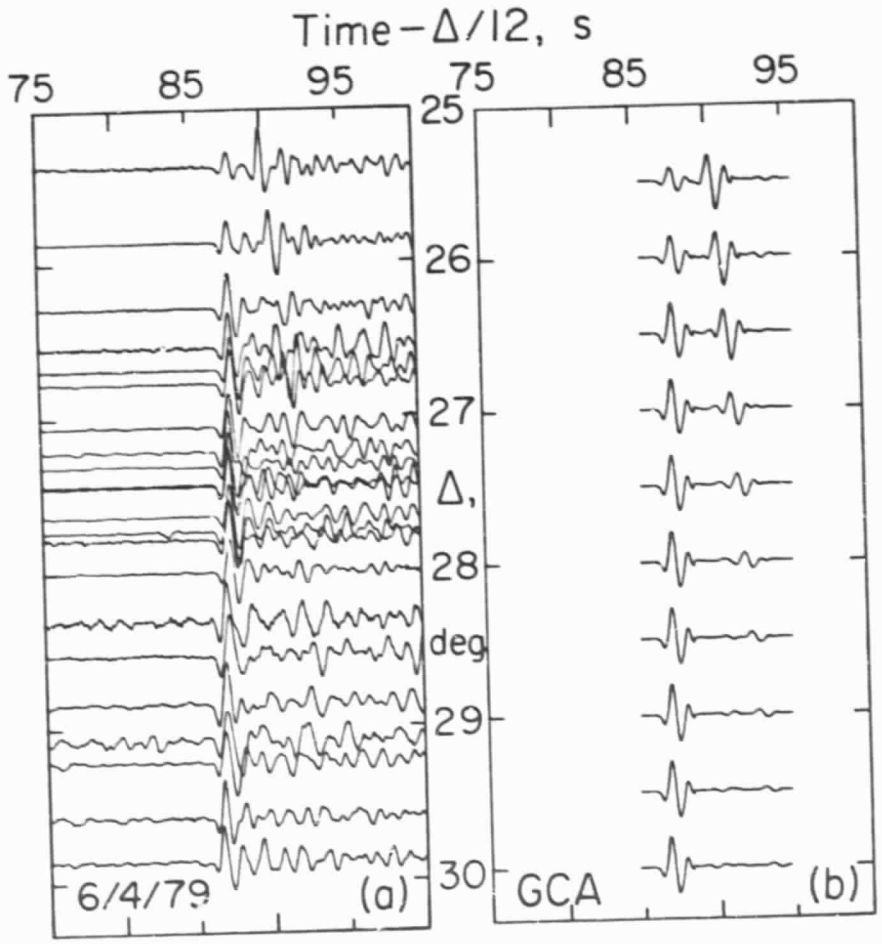

Fig. 6

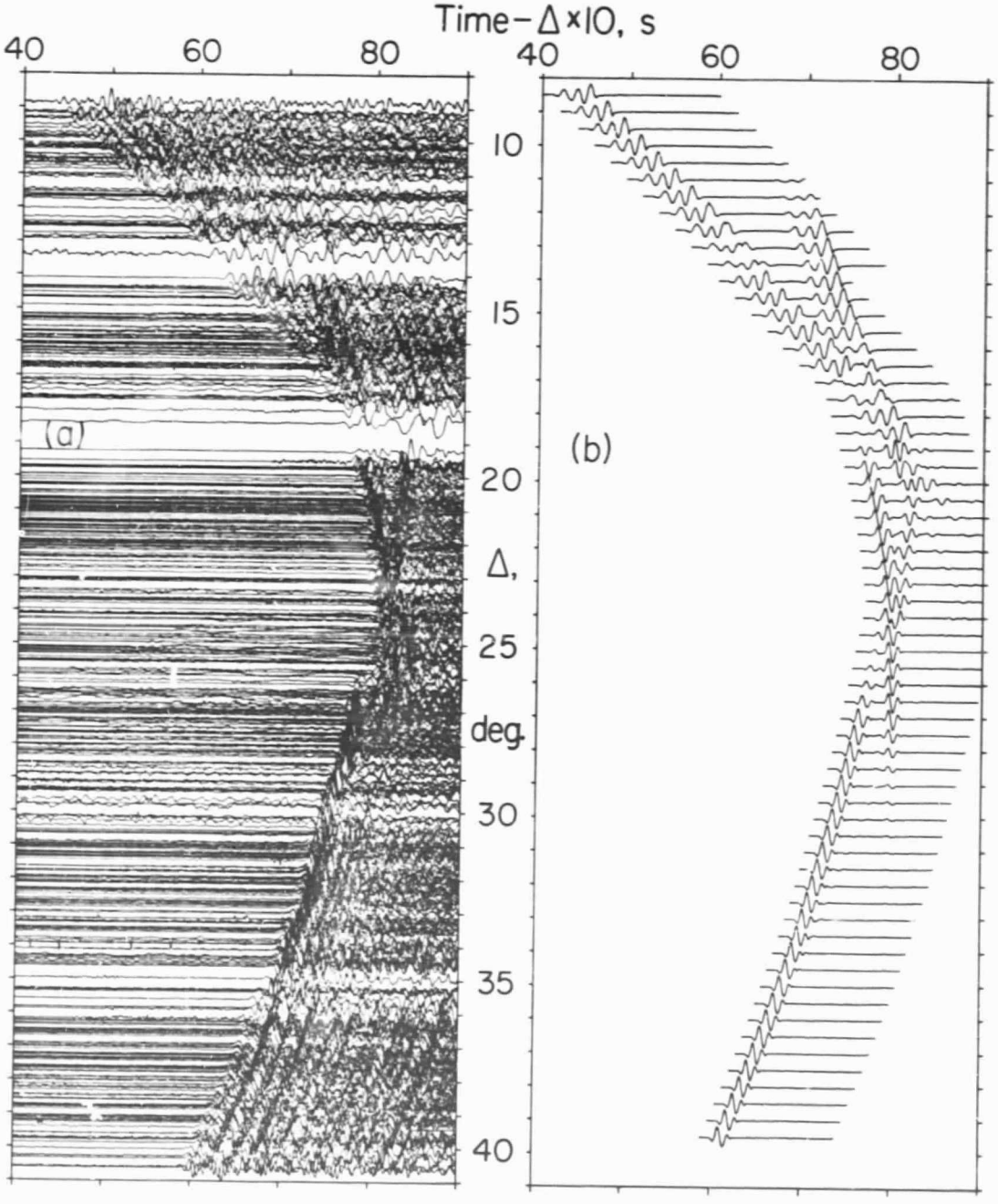

Fig. 7

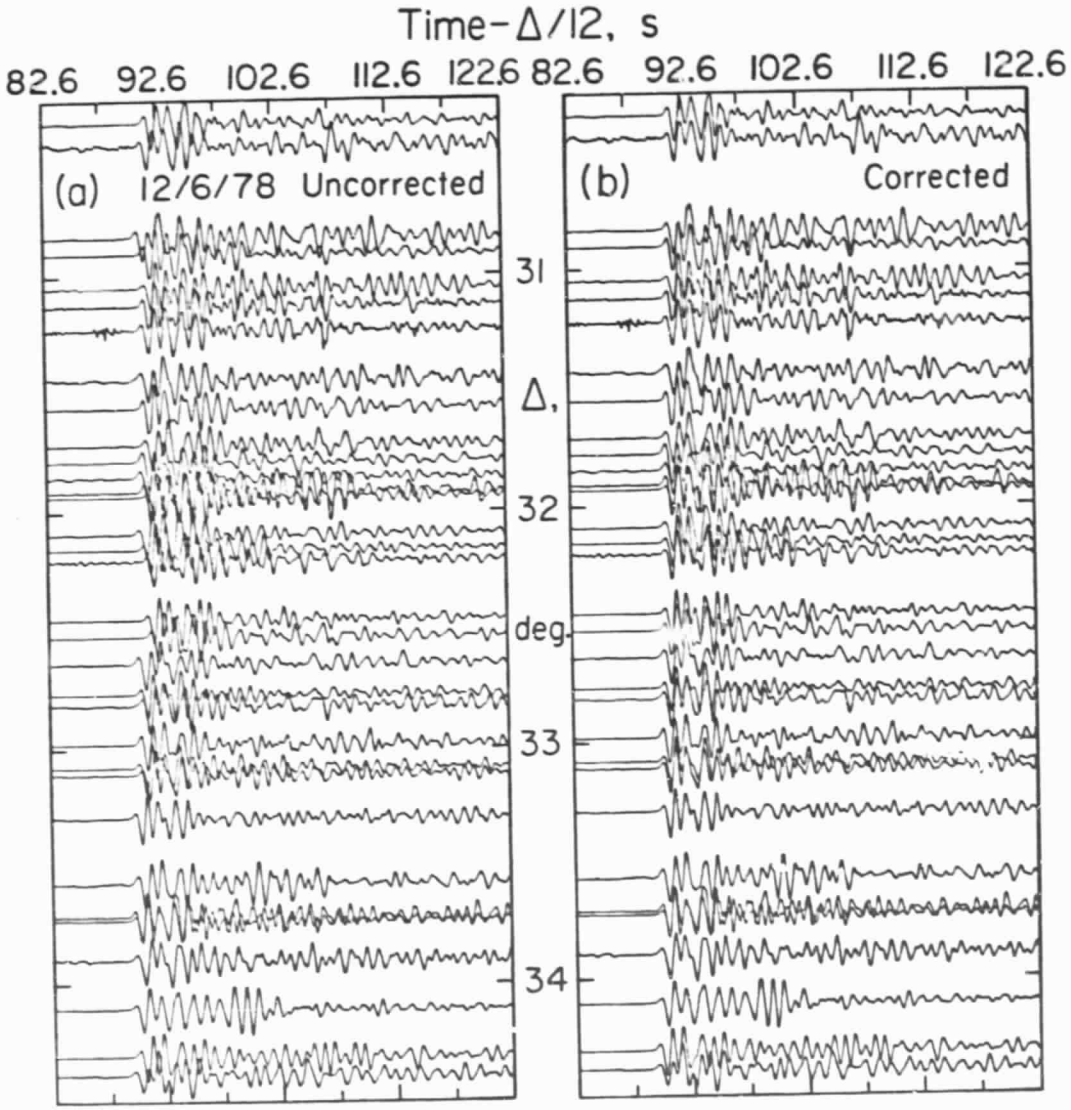

Fig. 8

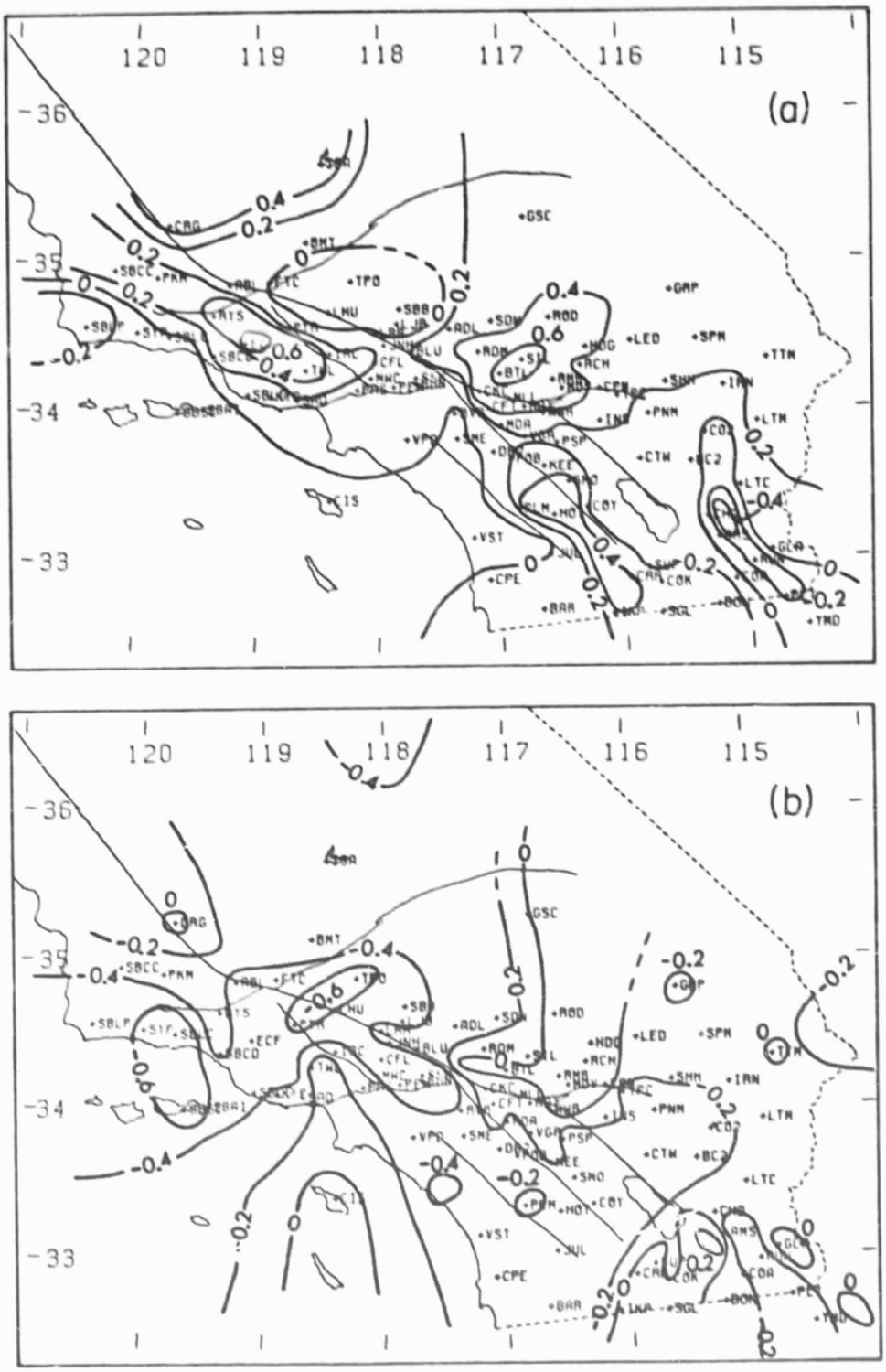

Fig. 9

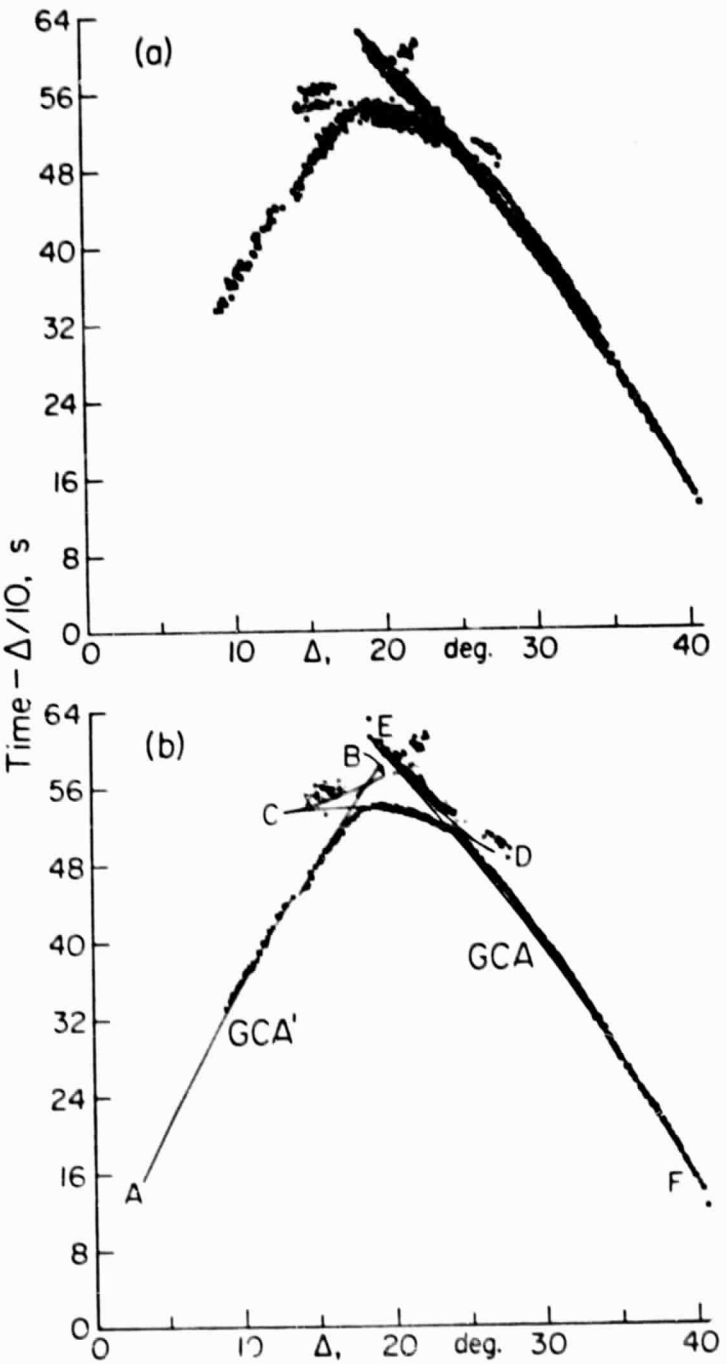

Fig. 10

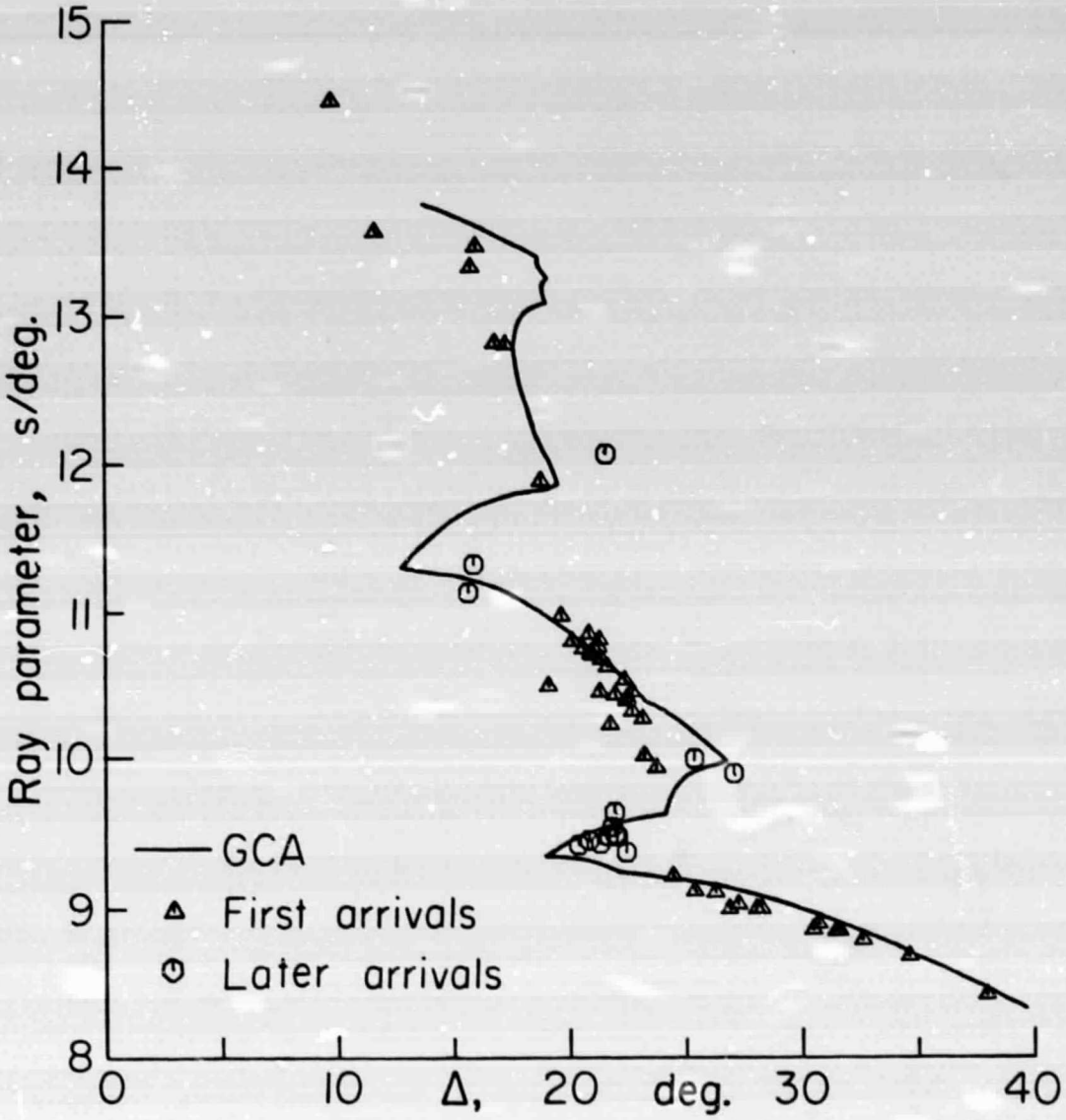

Fig. 11

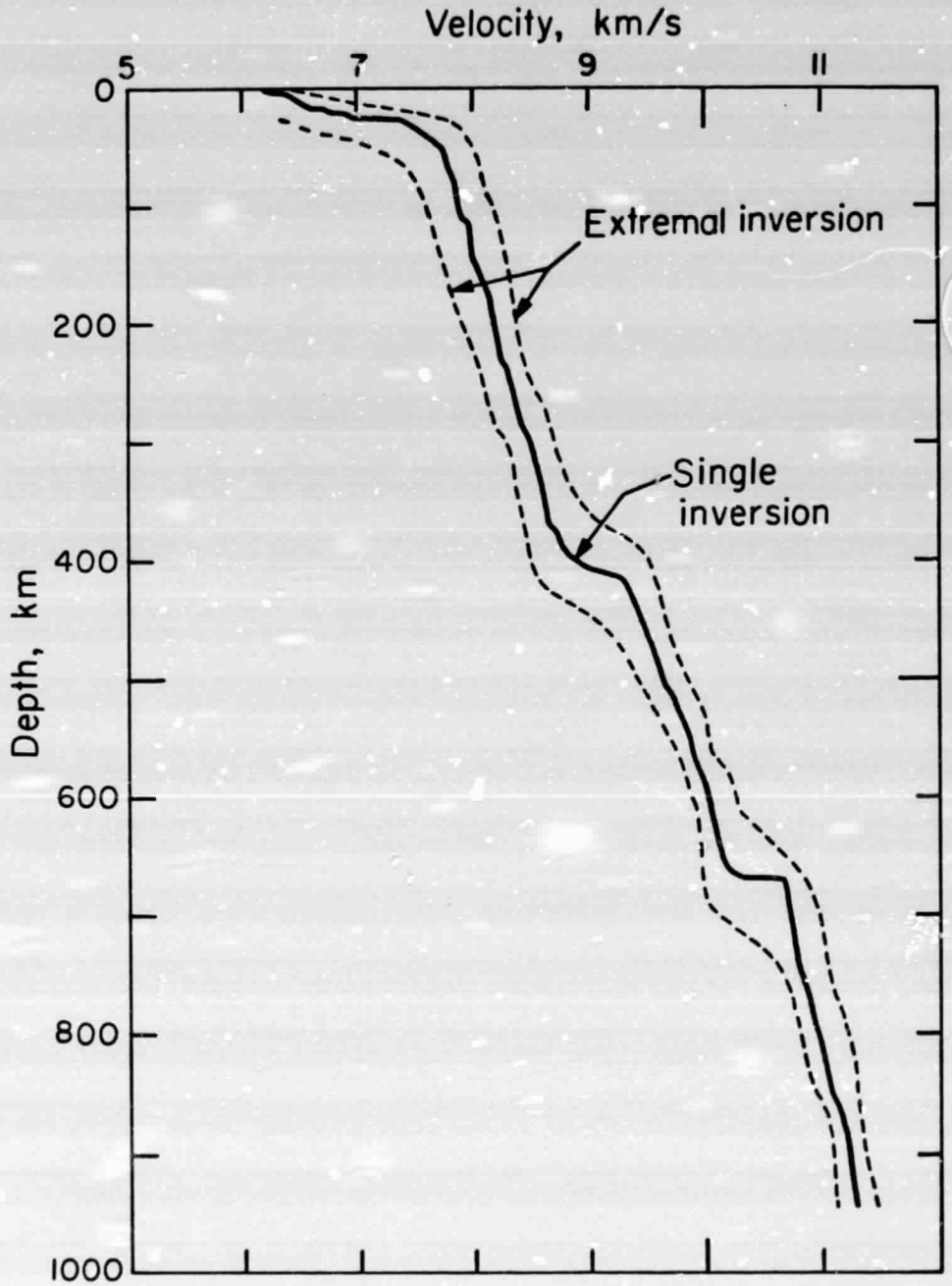

Fig. 12

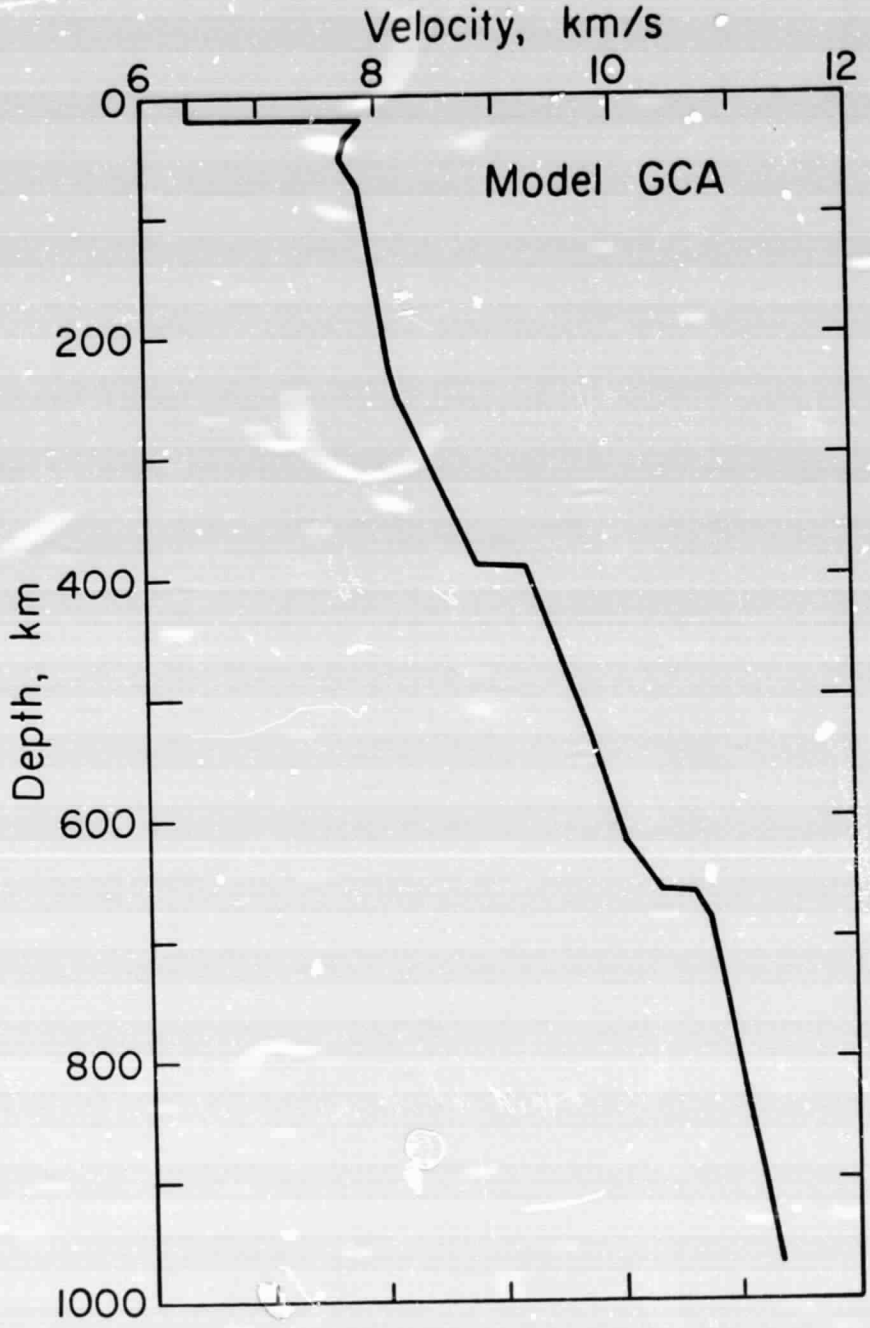

Fig. 13

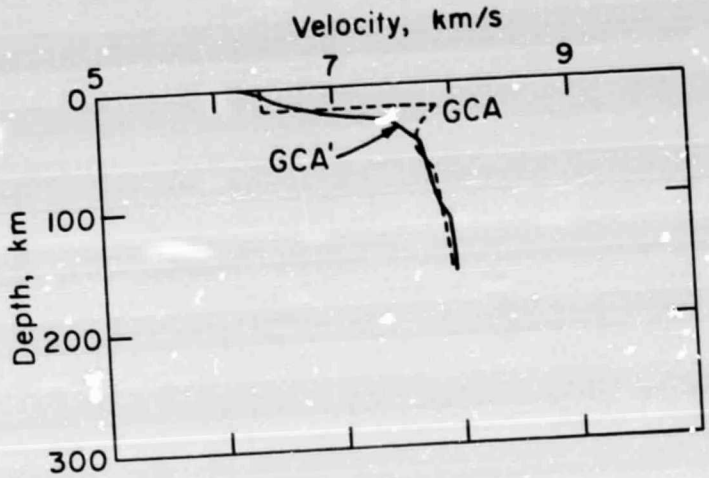

Fig. 14

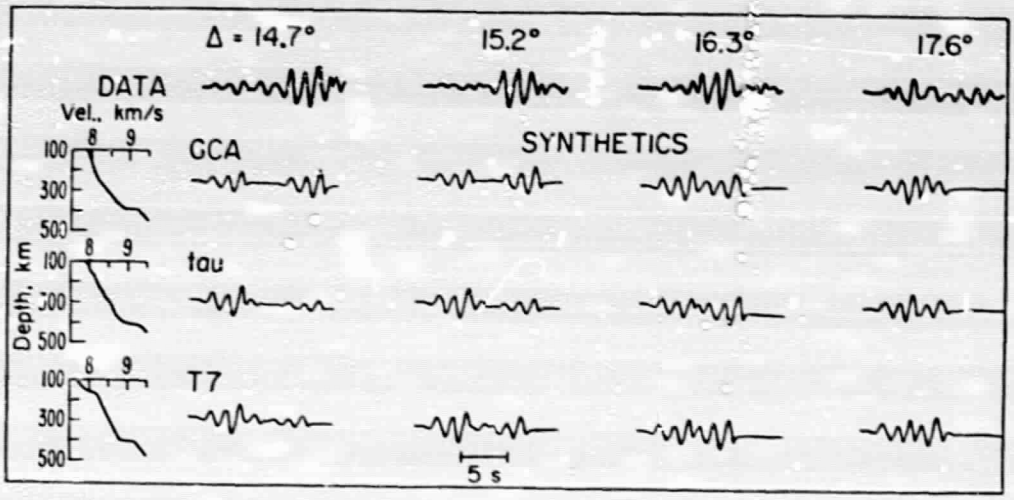

Fig. 15

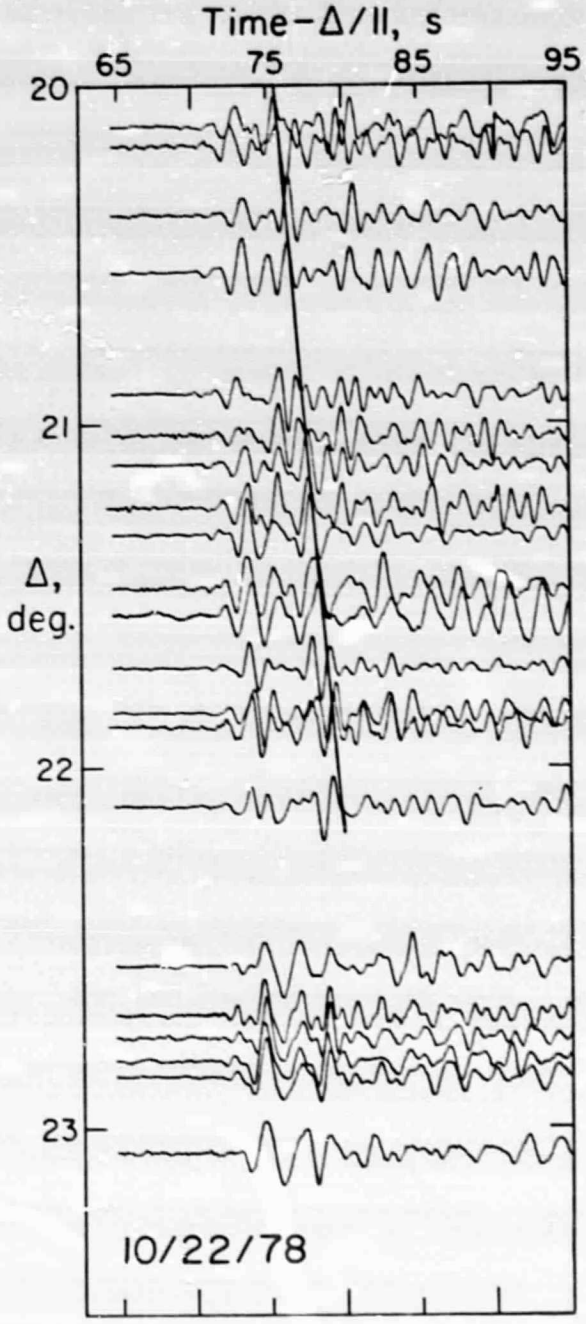

Fig. 16

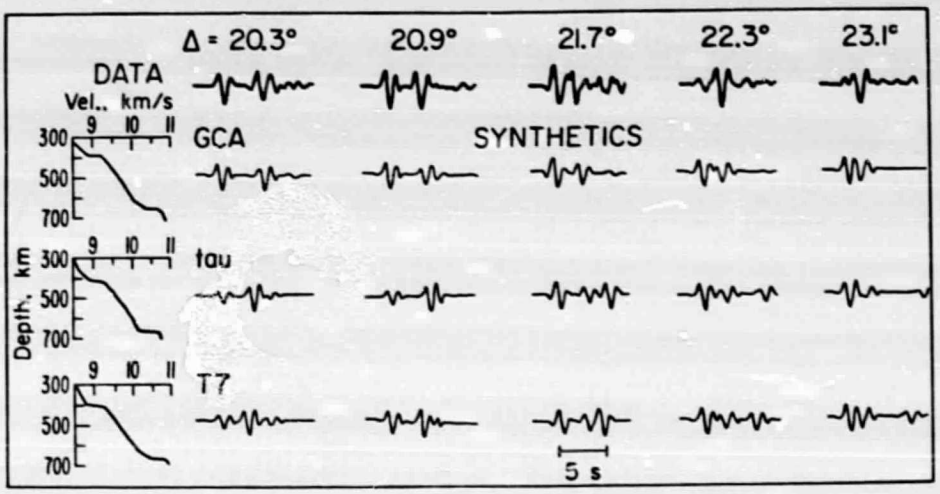

Fig. 17

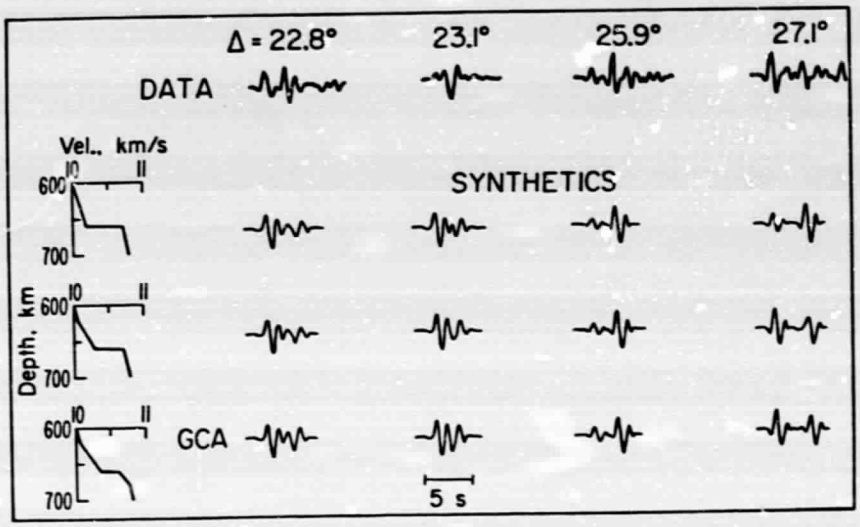

Fig. 18

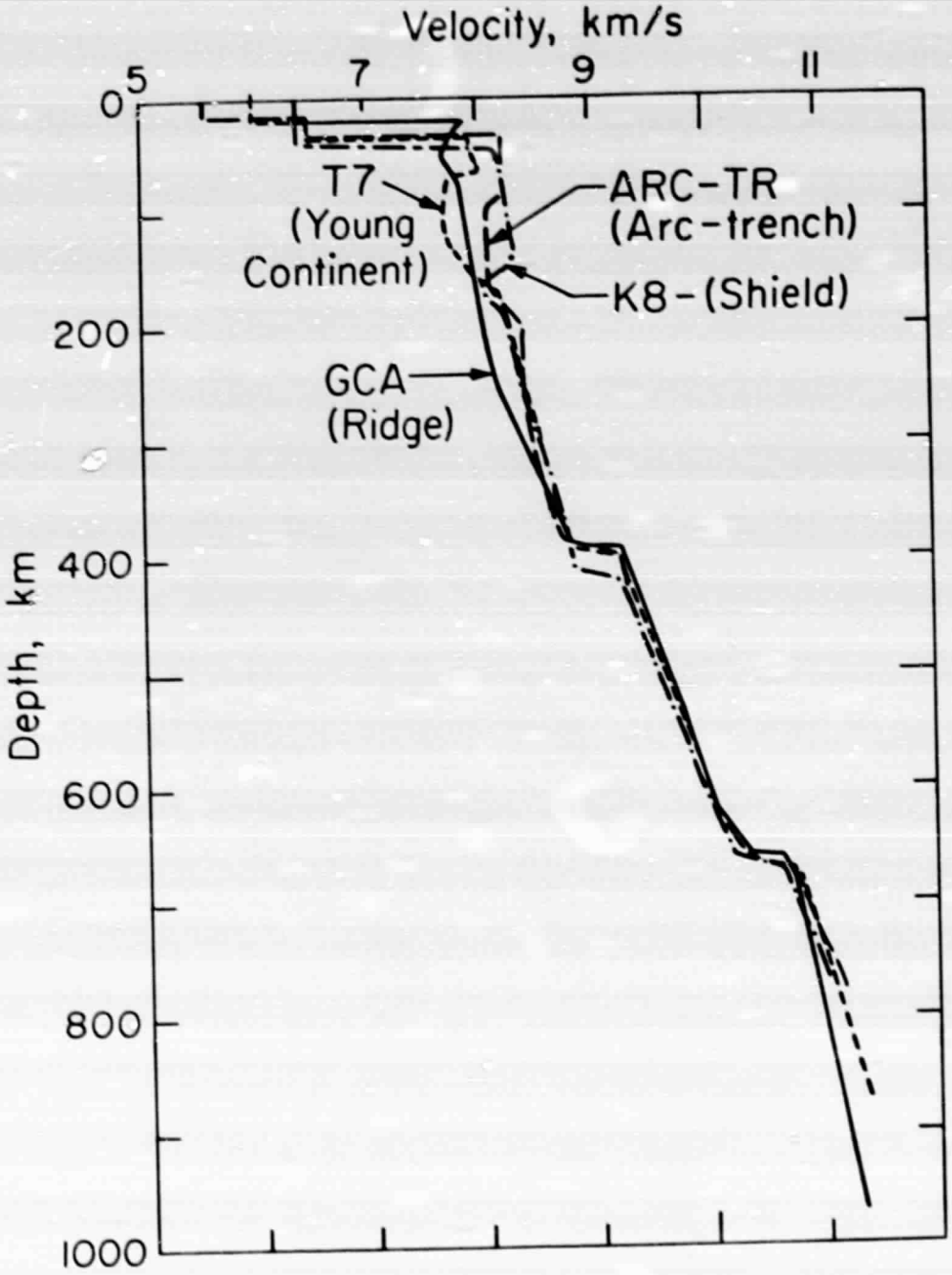

Fig. 19

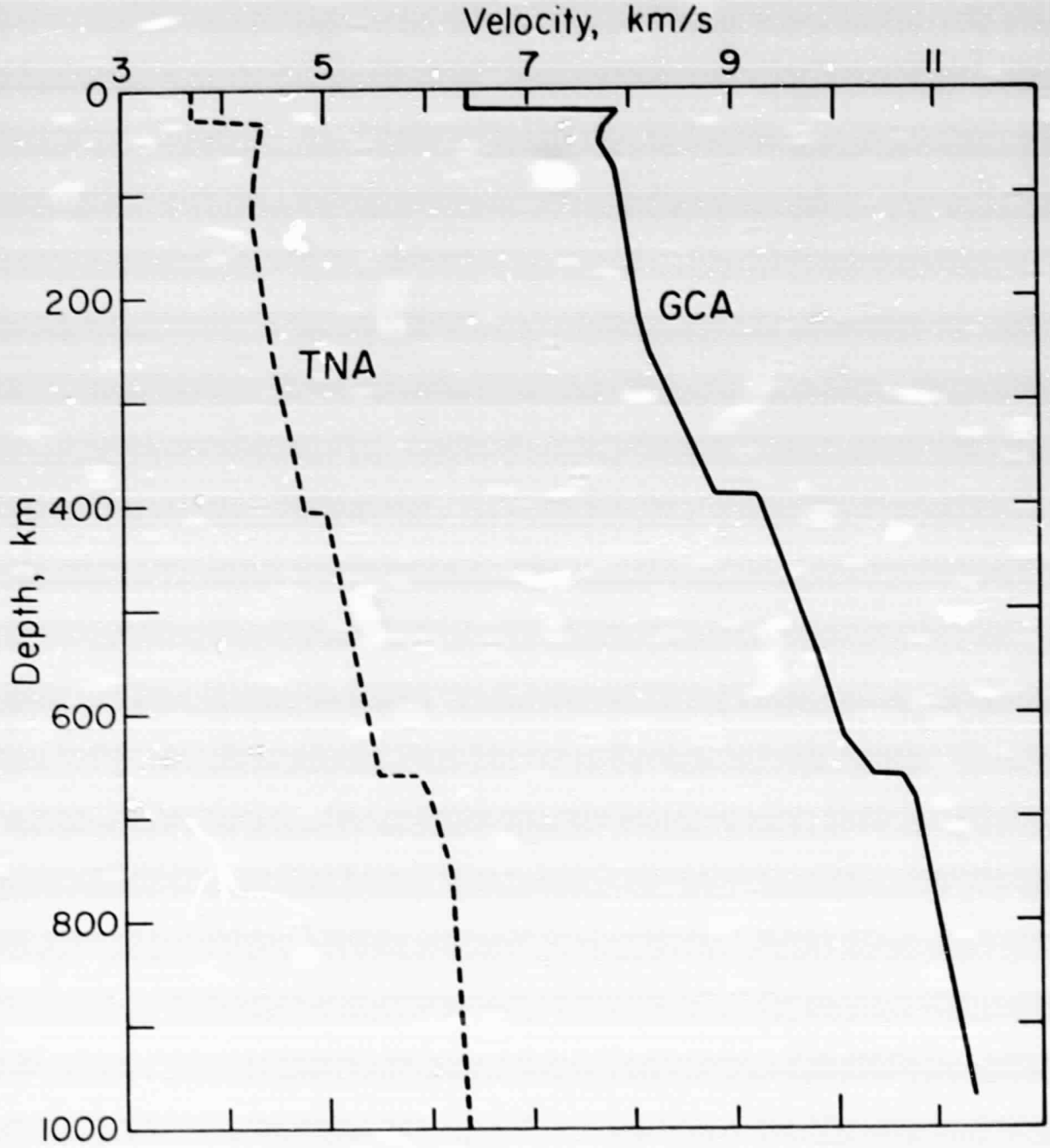

Fig. 20

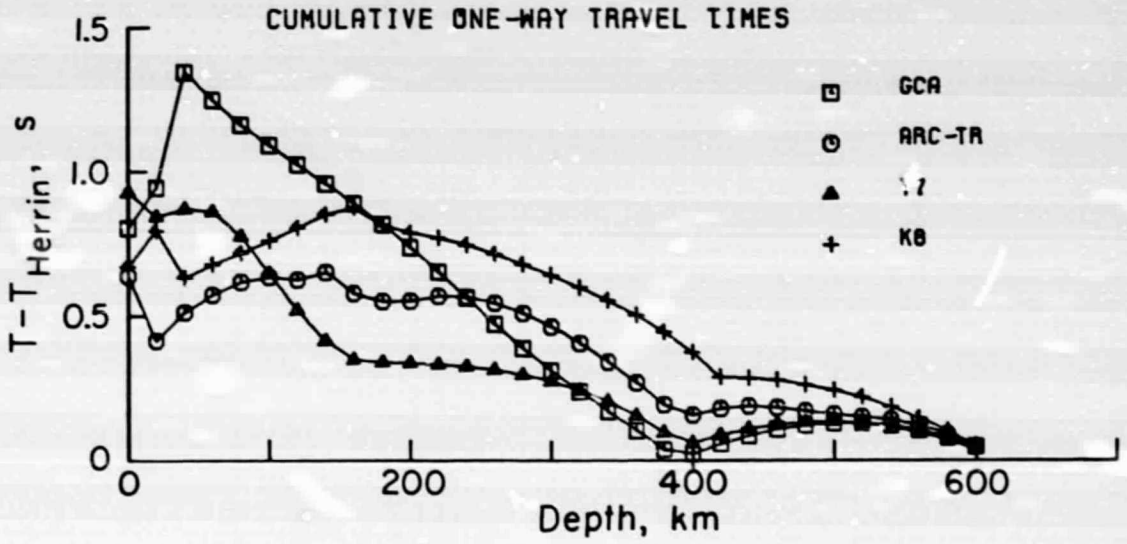

Fig. 21